

# Metal Halide Perovskite Nanowires: Synthesis, Integration, Properties, and Applications in Optoelectronics

Daquan Zhang, Qianpeng Zhang, Yiyi Zhu, Swapnadeep Poddar, Yuting Zhang, Leilei Gu, Haibo Zeng, and Zhiyong Fan\*

1D metal halide perovskite (MHP) nanowires (NWs) have energized research interest owing to their unique characteristics; they are grain-boundary-free, efficiently transport axial carriers, in conjunction with strong radial spatial confinement. Herein, recent progress in the synthesis, integration, property characterization, and advanced optoelectronic applications of MHP NWs is systematically reviewed. The approaches to synthesize MHP NWs are mainly classified into solution-phase and vapor-phase methods, as well as the top-down technique. Meanwhile, highly ordered patterns/templates-assisted and surface-guided alignment methods are utilized to integrate MHP NWs into NW arrays. The enhanced long-term stability and superior optoelectronic properties of MHP NWs enable excellent optoelectronic device performance, where solar cells, photodetectors, image sensors, bionic eyes, light-emitting diodes, resistive random-access memories, and field-effect transistors are mainly discussed. Finally, some perspectives for further direction of exploration to improve the device performance and path ways toward their practical applications are also provided.

## 1. Introduction

Metal halide perovskites (MHPs) possess a chemical formula of  $ABX_3$ , where A is a monovalent cation (e.g.,  $CH_3NH_3^+$  ( $MA^+$ ),  $NH_2CHNH_2^+$  ( $FA^+$ ), or  $Cs^+$ ), B is a divalent metal cation (e.g.,  $Pb^{2+}$ ,  $Sn^{2+}$ ), and X is a halide anion (e.g.,  $Cl^-$ ,  $Br^-$ ,  $I^-$  or mixed). The perovskite crystal structure provides a few exciting optoelectronic properties, namely, high absorption coefficient, low exciton binding energy, long carrier lifetime, high mobility, low defect density, high defect tolerance, strong radiative recombination, and tunable bandgaps covering the whole visible range.<sup>[1–12]</sup> The consequent high photon-to-electron conversion efficiency and vice versa make them promising candidates for next-generation high performance optoelectronic devices, such as solar cells,<sup>[13–22]</sup> photodetectors (PDs),<sup>[23–30]</sup> image sensors,<sup>[31–33]</sup> optically pumped lasers,<sup>[34,35]</sup>

and light-emitting diodes (LEDs),<sup>[36–42]</sup> ionizing radiation (X-ray and  $\gamma$ -ray) detection,<sup>[43–47]</sup> etc. For example, within one decade, the power conversion efficiency (PCE) and external quantum efficiency (EQE) of MHP solar cells and LEDs have reached up to 25.7%<sup>[14]</sup> and 25.6%<sup>[40]</sup> respectively, surpassing that of well-evolved alternatives, such as organic semiconductors, polycrystalline Si, CdTe, and CIGS.<sup>[15]</sup> Meanwhile, the facile synthesis of MHPs, such as low-temperature and solution processability, contributes to a meteoric rise in their commercial potential with a high performance-cost ratio.<sup>[48]</sup>

Recently, great effort has been made in obtaining MHPs with different morphologies, including bulk crystals,<sup>[44,49–53]</sup> thin films,<sup>[54–58]</sup> nanocrystals (NCs),<sup>[59–64]</sup> 2D crystals,<sup>[65–68]</sup> 1D nanowires (NWs),<sup>[32,33,69–74]</sup> and 0D quantum dots (QDs).<sup>[75–78]</sup> Among them, 1D NWs have garnered more research interests benefiting from their unique characteristics of grain-boundary-free, efficient axial carrier transportation, in conjunction with strong radial spatial confinement. Such a unique structure affects both the electron–hole and light–matter interactions, enabling novel photonic and optoelectronic properties.<sup>[79,80]</sup> Thereafter, significantly high performance has been achieved for MHP NWs-based optoelectronic devices. For example, a record responsivity value of  $2.6 \times 10^6$  A  $W^{-1}$  and detectivity value of  $7 \times 10^{15}$  Jones have been achieved for MHP NWs/graphene<sup>[81]</sup> and layered MHP NWs<sup>[82]</sup>-based devices, respectively. In addition, the polarized light emission<sup>[83]</sup> and detection<sup>[84]</sup> have also


D. Zhang, Q. Zhang, Y. Zhu, S. Poddar, Y. Zhang, Z. Fan  
Department of Electronic and Computer Engineering  
The Hong Kong University of Science and Technology  
Clear Water Bay, Kowloon, Hong Kong, SAR, China  
E-mail: eezfan@ust.hk

L. Gu  
Qingyuan Research Institute  
Shanghai Jiaotong University  
Shanghai 200240, China

H. Zeng  
MIIT Key Laboratory of Advanced Display Materials and Devices  
Institute of Optoelectronics and Nanomaterials  
College of Materials Science and Engineering  
Nanjing University of Science and Technology  
Nanjing 210094, China

Z. Fan  
Guangdong-Hong Kong-Macao Joint Laboratory for Intelligent  
Micro-Nano Optoelectronic Technology  
HKUST  
Clear Water Bay, Kowloon, Hong Kong, SAR, China

Z. Fan  
Department of Chemical and Biological Engineering  
The Hong Kong University of Science and Technology  
Clear Water Bay  
Kowloon, Hong Kong, SAR, China

 The ORCID identification number(s) for the author(s) of this article can be found under <https://doi.org/10.1002/aenm.202201735>.

DOI: 10.1002/aenm.202201735

been demonstrated in anisotropic MHP NWs. Given the promising potential for the next generation of high-performance optoelectronics, the systematic exploration of MHP NWs from the synthesis to devices is of great importance to underpin and promote its future applications.

Hence, in this review, we summarize recent progress about the synthesis, integration, property characterization, and advanced optoelectronic applications of MHP NWs, and provide perspectives on this exciting and rapidly developing research genre. In Section 2, we introduce the synthesis of MHP NWs, including solution-phase and vapor-phase approaches with and without physical templates, as well as the top-down technique. We then highlight the MHP NWs integration approach for preparing NW arrays in Section 3. After that, the physical and chemical properties of MHP NWs are discussed in Section 4, with a particular focus on the humidity- and phase-stability, along with unique optical properties. Subsequently, we give an overview of the optoelectronic applications of MHP NWs, including solar cells, PDs, image sensors and bionic eyes, LEDs, resistive random-access memories (Re-RAMs), and field-effect transistors (FETs). Finally, we provide a perspective to project the future development of MHP NWs and their integration into high-performance optoelectronics.

## 2. Synthesis of MHP NWs

As one of the most remarkable advantages over other semiconductor NWs, the MHP NWs can be easily fabricated by various methods, including solution-phase synthesis, vapor-phase growth, and top-down technique. Generally speaking, the solution process, with and without geometrical confinement, exhibits the advantages of high yield, large area, low-temperature processibility, substrate independence, and flexible device compatibility. The vapor-phase growth under a higher temperature contributes to high crystal quality and lower defect density, preferred for high-performance optoelectronic devices. Unlike the two bottom-up strategies mentioned above, top-down technique fabricates the NWs from the as-obtained MHP thin film with micromachining. Such a direct-patterning process demonstrates a simplified approach but high precision in controlling the dimension, resolution, and alignment of NW arrays. To compare the merits, recent progress for every method will be explicitly reviewed as followings.

### 2.1. Solution-Phase Method

#### 2.1.1. Self-Assembly Crystallization

Self-assembly crystallization has been demonstrated to be an effective strategy to synthesize nanomaterials, e.g., NWs, NCs, QDs, etc., not only for traditional semiconductors but also for MHPs. For example, Tong et al. developed a single-step ligand-mediated synthesis of all-inorganic ( $\text{CsPbX}_3$ ) perovskite NWs (Figure 1a).<sup>[85]</sup> Specifically, the  $\text{CsPbBr}_3$  NWs, which had a uniform diameter of 12 nm, were obtained from the oriented-assembly of the initially formed  $\text{CsPbBr}_3$  NCs with the assistance of organic ligands. Since the  $\text{CsPbCl}_3$  and  $\text{CsPbI}_3$  NWs

could not be synthesized directly using this method, a well-known halide ion exchange reaction from  $\text{CsPbBr}_3$  NWs was utilized to obtain different halide perovskite NWs with emission colors across the whole visible range. A similar assembling strategy has also been reported by Teunis et al.<sup>[86]</sup> In this work, ultrathin  $\text{MAPbBr}_3$  NWs with a diameter of  $\approx 3.8$  nm, namely, quantum wires (QWs), were obtained by assembling ultrasmall spherical  $\text{MAPbBr}_3$  NCs formed through dipolar interactions, as confirmed by the transmission electron microscopy (TEM) image in Figure 1b (bottom). Horváth et al., for the first time, reported a simple slip-coating synthesis of two sets of  $\text{MAPbI}_3$  NWs with mean diameters of 50 and 400 nm, and lengths up to 10  $\mu\text{m}$  (Figure 1c).<sup>[87]</sup> The  $\text{MAPbI}_3$  precursor solution was dropped onto a glass slide that was subsequently covered by another slide. While gradually sliding the upper one, the solvent evaporation from the uncovered surface caused the crystallization process and hence the NWs formation. Note that the whole crystallization process occurred at room temperature, which could further bring down the fabrication cost. Similarly, Deng et al. demonstrated a low-cost blade-coating method for obtaining single-crystalline  $\text{MAPbI}_3$  NWs on a hot (100 °C) substrate, as shown in Figure 1d. Upon solvent exposure and evaporation,  $\text{MAPbI}_3$  molecules precipitated out to form nuclei and aggregated along the triple-phase contact line. With the blade gradually receding, additional  $\text{MAPbI}_3$  molecules continuously flowed toward the growing nuclei and grew preferentially to form aligned NWs under the strong intermolecular interactions between adjacent  $\text{MAPbI}_3$  molecules. Gao et al. demonstrated an even more straightforward drop-coating method to fabricate  $\text{MAPbI}_3$  NW arrays on a 10° slope glass substrate.<sup>[84]</sup> The growth mechanism was the similar solvent evaporation,  $\text{MAPbI}_3$  precipitation, and crystallization processes. Some scanning electron microscopy (SEM) images of the as-obtained NWs are shown in Figure 1e. However, different from the blade-coating strategy, more substantial NWs diameter variation (from 100 nm to 2  $\mu\text{m}$ ) can be observed with the drop-coating method. A similar drop-coating method was also explored by Deng et al. to synthesize perovskite NWs on different substrates with well-controlled morphology.<sup>[88,89]</sup> Petrov et al. pioneered an intermediate phase-assisted growth process for perovskite NWs, where  $\text{MAI-PbI}_2\text{-DMF}$  or  $\text{FAI-PbI}_2\text{-DMF}$  acted as a structure-directing agent during the conversion to perovskite (Figure 1f).<sup>[90]</sup> It was found that the MAI or FAI concentration in isopropanol with the addition of DMF obviously affected the grown perovskite morphology. For example, an increase in the MAI concentration led to shorter NWs and slower color change of the films. Such a counterintuitive phenomenon could be attributed to the surface blocking effect. Meanwhile, 1% of DMF was enough to trigger NW shape rather than the cubic morphology produced in the absence of DMF, while an increase of DMF resulted in thicker NWs forming denser and smoother films. Hot-injection method, one of the most effective synthesis approaches for nanomaterials, was also explored for perovskite NWs.<sup>[70,91–93]</sup> For instance, Zhang et al. obtained single-crystalline orthorhombic  $\text{CsPbX}_3$  (X = Br, or I) NWs with uniform growth direction by reacting cesium oleate with lead halide in the presence of oleic acid and oleylamine in octadecene at 150–250 °C.<sup>[70]</sup> Under optimized reaction conditions, NWs with diameters uniformly below 12 nm and lengths

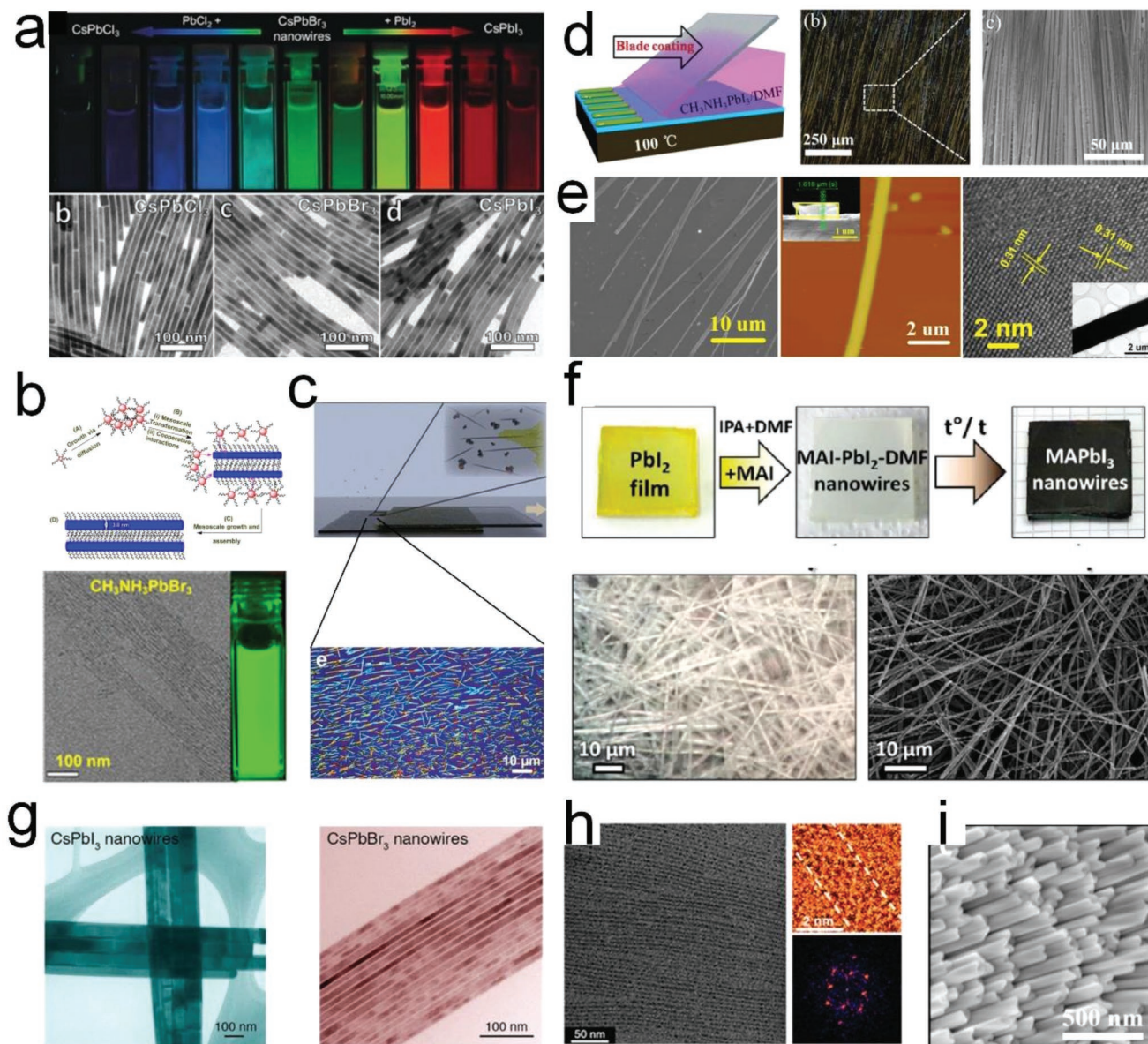


**Figure 1.** Solution-based template-free MHP NWs growth. a) One-step sonication assembly method: photograph of colloidal dispersions of CsPbX<sub>3</sub> NWs under UV irradiation (top), and TEM images of CsPbX<sub>3</sub> NWs (bottom). Reproduced with permission.<sup>[85]</sup> Copyright 2017, John Wiley and Sons. b) Ligand-assisted self-assembly method: Schematic illustration of the self-assembly process (top), TEM image (bottom-left), and UV-irradiated photograph (bottom-right) of MAPbBr<sub>3</sub> NWs. Reproduced with permission.<sup>[86]</sup> Copyright 2016, American Chemical Society. c) Slip coating method: schematic illustration of the slip coating process for the MAPbI<sub>3</sub> NWs fabrication (top), and optical microscopy image of the grown MAPbI<sub>3</sub> NWs (bottom). Reproduced with permission.<sup>[87]</sup> Copyright 2014, American Chemical Society. d) Blade coating method: schematic illustration of the blade coating process for MAPbI<sub>3</sub> NWs fabrication (left), optical microscope (middle), and SEM (right) images of the fabricated NW arrays. Reproduced with permission.<sup>[33]</sup> Copyright 2016, John Wiley and Sons. e) Drop-coating method: SEM image of MAPbI<sub>3</sub> NW arrays (left), AFM image of a single MAPbI<sub>3</sub> NW (middle), and HRTEM image of MAPbI<sub>3</sub> NW (right). Reproduced with permission.<sup>[84]</sup> Copyright 2016, American Chemical Society. f) Structure directing adduct-assisted method: photographs of the chip after different steps (top), an optical microscopy image of the intermediates of MAI-PbI<sub>2</sub>-DMF NWs (bottom-left), and SEM image of the final MAPbI<sub>3</sub> NWs (bottom-right). Reproduced with permission.<sup>[90]</sup> Copyright 2017, American Chemical Society. g–i) Hot injection methods: (g) TEM images of the grown CsPbBr<sub>3</sub> (left) and CsPbI<sub>3</sub> (right) NWs. Reproduced with permission.<sup>[70]</sup> Copyright 2015, American Chemical Society. h) Low-magnification TEM image (left), false-colored HRTEM image (top-right), and corresponding diffractogram (bottom-right) of the grown CsPbBr<sub>3</sub> NWs. Reproduced with permission.<sup>[92]</sup> Copyright 2016, American Chemical Society. (i) SEM image of the grown CsPbI<sub>3</sub> NRs. Reproduced with permission.<sup>[91]</sup> Copyright 2018, American Chemical Society.

up to 5 μm could be obtained (Figure 1g). The same group demonstrated similar method to grow ultrathin CsPbBr<sub>3</sub> QWs with diameter of 2.2 ± 0.2 nm and length up to several micrometers

(Figure 1h), where strong quantum confinement effect contributed to a high photoluminescence quantum yield (PLQY) value of the QWs.<sup>[92]</sup> Yang et al. obtained much thicker (≈150 nm

in diameter) CsPbI<sub>3</sub> nanorods (NRs) ( $\approx 2 \mu\text{m}$  in length) with the utilization of hot-injection method (Figure 1i).<sup>[91]</sup> The high crystal quality contributed to excellent photodetection performance in the NRs-based PDs.

### 2.1.2. Geometrically Confined Crystallization

Various templates have been utilized to geometrically confine the crystallization process to grow perovskite NWs, which can precisely control the obtained NWs diameter and length. For

example, Zhou et al. reported a unique self-template-directed fabrication of MAPbBr<sub>3</sub> NWs, by reacting the Pb-containing precursor NWs with MABr and HBr in an organic solvent at room temperature, as shown in Figure 2a.<sup>[94]</sup> Interestingly, the release of the organic component of the precursor Pb-containing NWs results in the formation of mesopores in the perovskite NWs. Anodic aluminum oxide (AAO) templates comprising vertically aligned nanochannels have also been demonstrated widely for the solution-phase MHP NWs fabrication.<sup>[95–106]</sup> Since the AAO fabrication has excellent structure engineering capability, such a fabrication process for perovskite

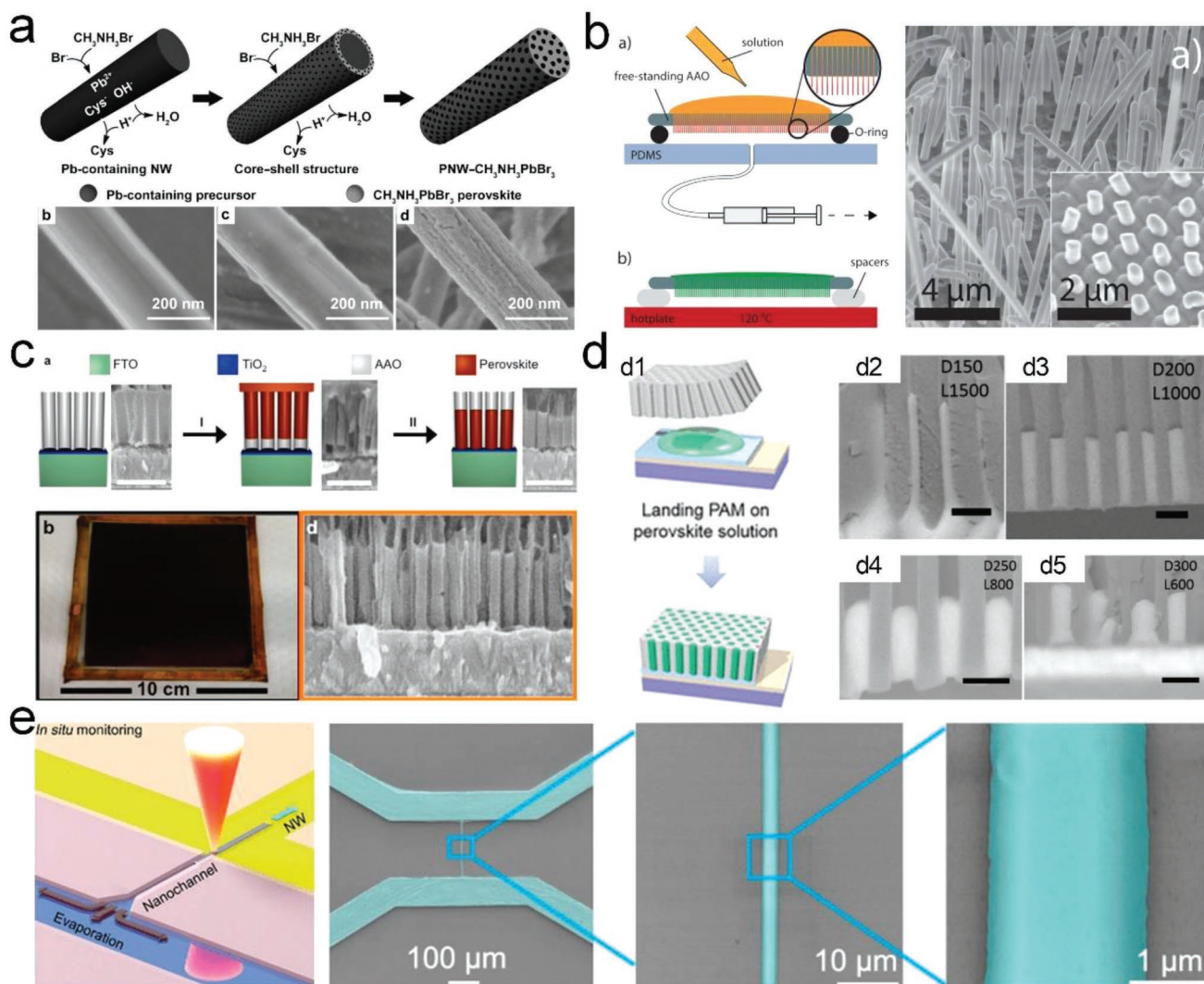


**Figure 2.** Solution-based template-assisted MHP NWs growth. a) Self-templating method: schematic illustration of the synthesis of porous MAPbBr<sub>3</sub> NWs (top), and SEM images of the intermediates at different reaction times (bottom). Reproduced with permission.<sup>[94]</sup> Copyright 2015, John Wiley and Sons. (b–d) AAO templates-assisted fabrication methods: (b) schematic illustration of extruding MAPbBr<sub>3</sub> NWs out from the AAO template (left), and SEM images of the obtained MAPbBr<sub>3</sub> NWs (right). Reproduced with permission.<sup>[95]</sup> Copyright 2017, American Chemical Society. (c) Schematic illustration of the fabrication process (top), a photograph of a  $\approx 9 \times 9 \text{ cm}$  NW array (bottom-left), and SEM image (bottom-right) of the MAPbI<sub>3</sub> NWs in AAO template by dissolution and recrystallization processes. Reproduced with permission.<sup>[96]</sup> Copyright 2016, American Chemical Society. (d) Capillary effect assisted MHP NW arrays in AAO template: schematic illustration of the fabrication process (d1), and SEM images of MHP NW arrays in AAO templates with different diameters and pitches (d2–d5). Reproduced with permission.<sup>[103]</sup> Copyright 2020, American Chemical Society. (e) Micro/nanofluidic fabrication technique (MNFFT) for MAPbI<sub>3</sub> NWs growth: schematic illustration (left) and SEM images of the fabricated NW under different magnifications (right). Reproduced with permission.<sup>[107]</sup> Copyright 2018, American Chemical Society.

NWs, has an obvious advantage in controlling the geometry, compared with the methods discussed above. For example, Oener et al. obtained vertically freestanding MAPbBr<sub>3</sub> NWs by extruding the precursor solution through the through-pore AAO template (Figure 2b).<sup>[95]</sup> Even though no NWs-based device was demonstrated, the obtained perovskite NWs were shown to have excellent photophysical properties, such as high PLQY and low surface recombination velocity, which would be a promising candidate for integration in optoelectronic devices. Similar perovskite precursor filling and crystallization within the AAO template have also been reported by many groups. For instance, Ashley et al. for the first time demonstrated the perovskite NWs growth within AAO templates by directly dropping the precursor solution onto the AAO template (Figure 2c).<sup>[96]</sup> To remove the residual perovskite thin film, a surface-cleaning step where a syringe pump dispensed a solution of DMSO and chlorobenzene on the top of the rapidly rotating AAO template was conducted after crystallization. It is attractive that a large area (9 × 9 cm<sup>2</sup>) NW array can be obtained with such a method, as shown in Figure 2c. Some other techniques, such as inkjet printing,<sup>[97,98]</sup> spin-infiltration,<sup>[99–101]</sup> and capillary infiltration,<sup>[102,103]</sup> were also integrated with the AAO template for the perovskite NWs fabrication. For instance, Zhang et al. obtained perovskite NWs by using an AAO template membrane to cover perovskite precursor solution on a substrate, where the capillary effect forced the solution to go into AAO nanopores to form NW arrays (Figure 2d).<sup>[103]</sup> In addition to AAO templates, other templates have also been utilized to fabricate perovskite NWs. For example, Zhou et al. reported a micro/nanofluidic fabrication technique for perovskite NWs growth, which enabled both precise control and in situ monitoring of the NWs growth (Figure 2e).<sup>[107]</sup> Spina et al. reported a similar open nanofluidic channel assisted growth of perovskite NWs.<sup>[108]</sup> Meanwhile, more poly(dimethylsiloxane) (PDMS) and photoresistor templates for the perovskite NWs growth will be discussed in the integration of NW arrays part (Section 3).

## 2.2. Vapor-Phase Method

Vapor-phase growth of MHP NWs under elevated temperatures usually leads to high crystal quality and lower defect density, which are highly desired in multifarious optoelectronic applications, including but not limited to high-performance PDs, LEDs, lasers, and Re-RAMs for future data storage and neuromorphic computing.<sup>[109]</sup> It can be subdivided into vapor-liquid-solid (VLS) and vapor-solid (V-S) processes. Meng et al. reported for the first time the VLS technique of growing all-inorganic monocrystalline perovskite NWs on SiO<sub>2</sub>/Si substrate, utilizing Sn as catalysts.<sup>[110]</sup> The growth process has been schematically illustrated in Figure 3a (left), where the predeposited liquid Sn catalyst supersaturates over time upon temporally reacting with gaseous perovskite species like Cs, Pb, and halide. The diameter of the Sn-droplet can determine the diameter of the NWs, as confirmed by the TEM energy dispersive spectroscopy (EDS) in the right of Figure 3a. In another notable work on VLS synthesis of MHP NWs, Meyers et al. reported a self-catalysis approach where Pb in the liquid phase

was supersaturated first to grow a lead halide NW, following which low-temperature reaction with organohalide precursor rendered the NW to metamorphose to that of MHP.<sup>[111]</sup> The phase diagram depicting such a growth process is provided in Figure 3b1,b2. Figure 3b3 shows the SEM images of the PbI<sub>2</sub> and MAPbI<sub>3</sub> NWs, and the PL mapping of a MAPbI<sub>3</sub> NW is shown in Figure 3b4. A chemical vapor transport process was reported by Park et al., where template-free single-crystalline CsPbX<sub>3</sub> NWs could be assembled vertically without template support (Figure 3c).<sup>[112]</sup> Meanwhile, an intriguing technique of growing highly ordered vertically aligned ultra-high-density monocrystalline MHP NW and QW arrays was devised by Fan and co-workers, by fusing the template-assisted growth with the V-S process.<sup>[32,113–120]</sup> Since this growth process is generic, an assortment of MHP NWs has been fabricated, including MAPbX<sub>3</sub> (X = Cl, Br, or I), MASnI<sub>3</sub>, FAPbI<sub>3</sub>, CsPbI<sub>3</sub>. Specifically, electrodeposited Pb<sup>[32]</sup> or Sn<sup>[113]</sup> clusters in the nanochannels of AAO templates were made to react with perovskite precursor (AX, A = MA, FA, or Cs, X = Cl, Br, or I) vapor in a tubular furnace by a vapor–solid–solid-reaction (VSSR) process, as shown in Figure 3d. The fabricated MHP NWs and QWs offer a 100% filling ratio (Figure 3e)<sup>[116]</sup> and excellent single crystallinity (Figure 3f).<sup>[118]</sup> Utilizing the AAO templates with Pb clusters, the same group reported a close-spaced vapor reaction (CSVR) method to grow crystalline perovskite QW arrays, namely, NWs with diameters in the quantum regime, on 4-in. Si wafers, as shown in Figure 3g.<sup>[120]</sup> Interestingly, the perovskite QWs components can be easily tuned by changing the halide sources, resulting in the emission spectra covering the whole visible range (blue, cyan, green, and red). Another method of the V-S growth process was adopted by Oksenberg et al., where highly monocrystalline CsPbBr<sub>3</sub> NWs were fabricated by a surface-guided epitaxial technique via a chemical vapor deposition (CVD) process on C-plane sapphire substrate as shown in Figure 3h.<sup>[121]</sup> Shoaib et al. also reported epitaxial growth of ultralong (millimeter range) highly ordered CsPbBr<sub>3</sub> NWs on M-plane sapphire substrate.<sup>[71]</sup> The SEM and TEM images of such NWs have been provided in Figure 3i.

It is significant that VLS and epitaxial CVD processes can yield MHP NWs with precisely controlled crystalline orientation and growth direction. While, the template-assisted VSSR process offers a much higher integration density of the NWs with controllable diameters and lengths. Such VSSR-grown NWs become more meaningful in applications that require device scaling, lateral electrical isolation, large surface-to-volume ratio, as well as NWs geometry engineering. More vapor-phase growth of MHP NWs have also been reported by other groups.<sup>[122–127]</sup>

## 2.3. Top-Down Method

Figure 4 shows the top-down method for MHP NWs fabrication. Mao et al. reported the direct patterning of perovskite solid-state thin-films into periodic nanostructures, which helped with the improved light extraction and spontaneous emission rate of the perovskite LEDs, resulting in a twofold higher radiance compared to the planar counterpart (Figure 4a).<sup>[128]</sup> The imprinting was done with the own gravity of the PDMS mold when

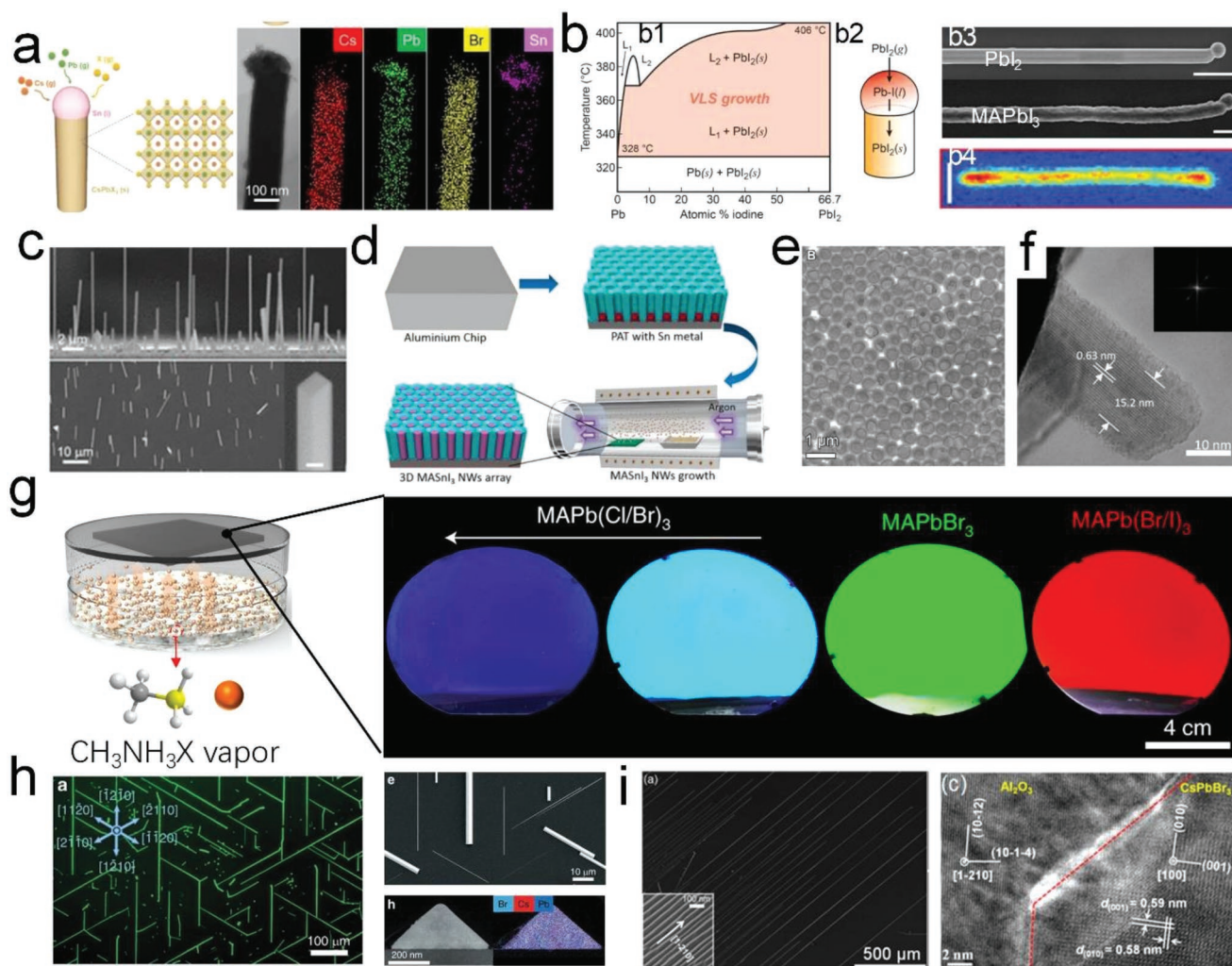


**Figure 3.** Vapor phase MHP NWs growth. a) Direct VLS growth of  $\text{CsPbX}_3$  NWs: schematic illustration of the VLS growth using the Sn catalysts (left), and the TEM image and EDS mappings of a single  $\text{CsPbBr}_3$  NW (right). Reproduced with permission.<sup>[110]</sup> Copyright 2019, American Chemical Society. b) VLS growth of  $\text{PbI}_2$  NWs and conversion to  $\text{MAPbI}_3$  NWs: the Pb-I binary-phase diagram (b1), schematic illustration of the VLS growth of  $\text{PbI}_2$  NWs (b2), SEM image of the grown  $\text{PbI}_2$  and  $\text{MAPbI}_3$  NWs (b3), and PL mapping of a  $\text{MAPbI}_3$  NW (b4). Reproduced with permission.<sup>[111]</sup> Copyright 2017, American Chemical Society. c) SEM images of vertically aligned  $\text{CsPbBr}_3$  NWs by CVD growth method. Reproduced with permission.<sup>[112]</sup> Copyright 2016, American Chemical Society. d) Schematic illustration of the VSSR growth of  $\text{MASnI}_3$  NWs in AAO templates. Reproduced with permission.<sup>[113]</sup> Copyright 2017, American Chemical Society. e) SEM image of the VSSR grown  $\text{MAPbCl}_3$  NWs in AAO template. Reproduced with permission.<sup>[116]</sup> Copyright 2020, American Association for the Advancement of Science. f) TEM image of a single  $\text{MAPbI}_3$  NW extracted out from AAO template. Reproduced with permission.<sup>[118]</sup> Copyright 2019, American Chemical Society. g) CSV growth method: schematic illustration of the growth (left) and PL image of  $\text{MAPbX}_3$  QWs grown on 4-in. wafers (right). Reproduced with permission.<sup>[120]</sup> Copyright 2022, Springer Nature Limited. h,i) Epitaxial CVD growth method: (h) optical PL image (left) and SEM/TEM images (right) of the grown  $\text{CsPbBr}_3$  NWs on C-plane sapphire substrate. Reproduced with permission.<sup>[121]</sup> Copyright 2020, Springer Nature Limited. (i) SEM image (left) and cross-sectional TEM image (right) of the grown  $\text{CsPbBr}_3$  NWs on annealed M-plane sapphire substrate. Reproduced with permission.<sup>[71]</sup> Copyright 2017, American Chemical Society.

perovskite thin film was placed in the MA vapor environment. The liquid intermediate was then converted to solid perovskite phase before detaching the PDMS mold. Moreover, Cao et al. reported the fabrication of MHP NW arrays by imprinting P(VDF-TrFE)/perovskite hybrid film with a commercially available DVD-R disk, as schematically shown in Figure 4b.<sup>[129]</sup> In their fabrication, the hybrid film was required to be thin and wet to obtain transparent NW arrays. The as-deposited film was imprinted immediately, followed by a gradient annealing process (50 °C for 5 min to volatilize the solvent, and 100 °C for 10 min to form large crystals).

Besides the nanoimprinting method discussed in the above two reports, focused-ion beam (FIB) etching has also been utilized to fabricate the wire-shaped gratings. For instance, Alias et al. reported the chemically gas-assisted FIB method to fabricate the perovskite subwavelength grating (SWG) absorber with  $\text{XeF}_2$  and  $\text{I}_2$  precursors (Figure 4c).<sup>[130]</sup> Alias et al. also reported the same method for acquiring both binary (Figure 4d) and circular SWGs.<sup>[131]</sup> Moreover, Gao et al. utilized e-beam lithography and inductively coupled plasma etching to form  $\text{MAPbBr}_3$  gratings and achieved different structure colors by tuning the grating period and gap width (Figure 4e).<sup>[132]</sup>

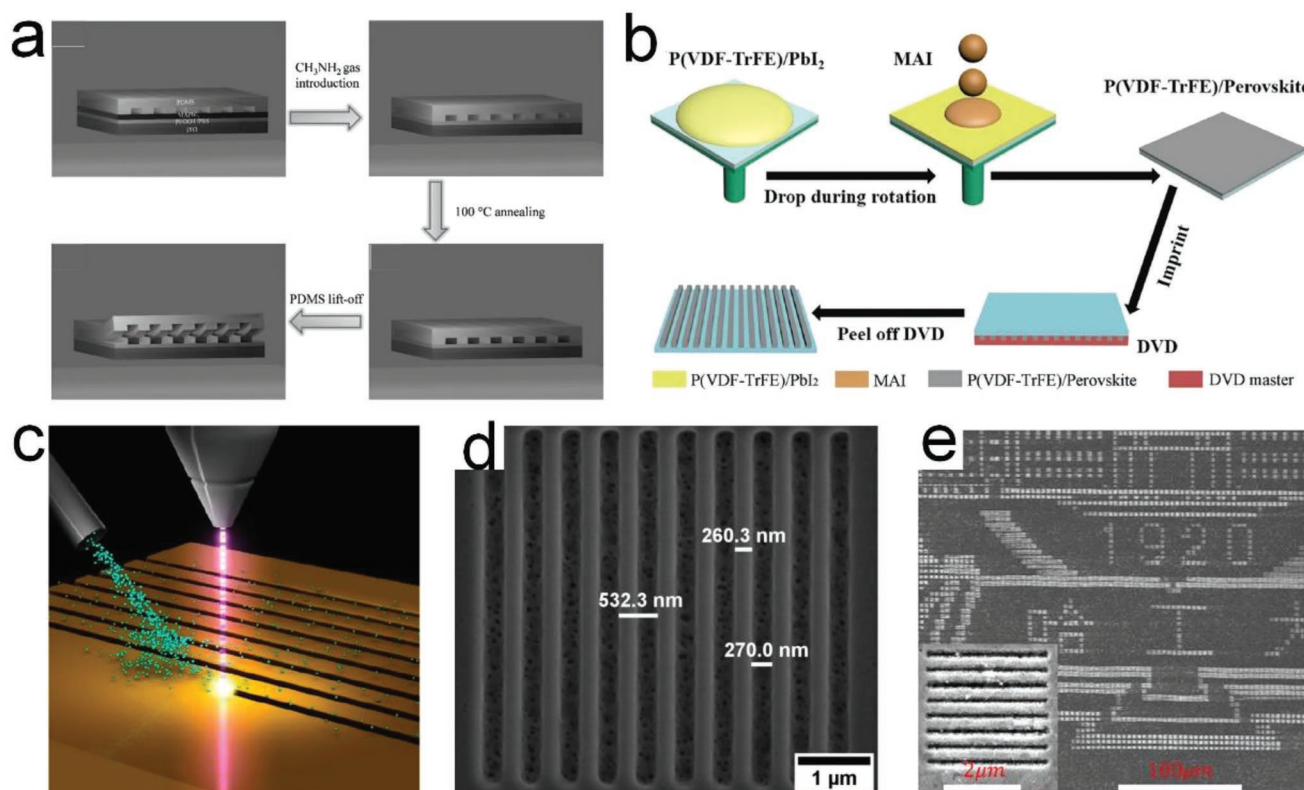


**Figure 4.** Top-down method for MHP NWs fabrication. a,b) Nanopatterning approach: (a) schematic illustration of the nanoimprinting process with the utilization of PDMS mask and MAI gas. Reproduced with permission.<sup>[128]</sup> Copyright 2017, John Wiley and Sons. b) Schematic illustration of the DVD master-assisted nanoimprinting process. Reproduced with permission.<sup>[129]</sup> Copyright 2019, John Wiley and Sons. c,d) FIB approach: (c) schematic illustration of the FIB process. Reproduced with permission.<sup>[130]</sup> Copyright 2015, American Chemical Society. (d) SEM image of the fabricated MAPbBr<sub>3</sub> grating. Reproduced with permission.<sup>[131]</sup> Copyright 2015, American Vacuum Society. (e) Electron-beam lithography approach: SEM image of the fabricated MAPbBr<sub>3</sub> nanopattern. Reproduced with permission.<sup>[132]</sup> Copyright 2018, American Chemical Society.

### 3. Integration of MHP NWs

Constructing NW arrays for scalable integration is highly desirable in the fields of nanophotonics, high-performance optoelectronics, and integrated circuits.<sup>[133–135]</sup> However, due to the instability associated with perovskites, conventional processing techniques for Si, such as photolithography, wet-etching, etc., are not suitable. Benefiting from easy crystallization and soft nature of perovskites, ordered MHP NW arrays have been demonstrated by various methods, such as the crystallization confinement in ordered patterns/templates, roll-to-roll (R2R) technique, asymmetric capillary force-assisted growth, 3D printing, and surface guided epitaxial CVD growth. Those methods will be classified into two categories, namely ordered patterns/template-assisted and surface-guided alignment, and they are systematically reviewed in this section.

#### 3.1. Ordered Patterns/Templates-Assisted Alignment

Various ordered patterns and templates, such as PDMS and photoresistors with nanopatterns, AAO, etc., have been used to perform ordered alignment of MHP NWs. For example, Jeong et al. utilized a patterned PDMS mold to make the perovskite precursor film moldable.<sup>[136]</sup> As shown in **Figure 5a**, After the

precursor thin film was spin-coated and formed a soft-gel state, the prepatterned PDMS mold was applied to fabricate the NW morphology. In order to provide sufficient fluidity of a thin precursor film at room temperature for efficient pattern formation, DMSO, a high-boiling point solvent, rather than DMF, was utilized for the precursor solution. Followed by 80 °C annealing treatment, the perovskite NW arrays could be formed, as shown by the SEM image in **Figure 5a**. Liu et al. directly put a PDMS pad with rectangular grooves onto a stock solution of perovskite precursor in DMF, without a spin-coating process.<sup>[137]</sup> Upon mild pressure (<20 KPa) on the PDMS pad, the solution was driven into the void space of PDMS templates. After slow evaporation of the solvent (2–3 h), nucleation occurred at the high surface-energy corners of the grooves which prompted the development of the gas–liquid–solid contact lines. After that, the nuclei grew rapidly (<20 s) along the longitudinal direction of the grooves, forming well-aligned perovskite NWs on the substrate. Yang et al. demonstrated similar PDMS templates for the perovskite NW arrays fabrication with an antisolvent-assisted crystallization process.<sup>[138]</sup> More PDMS templates for the well-aligned MHP NW arrays fabrication were also demonstrated by other groups.<sup>[139–142]</sup> Apart from the microprinting method discussed above, using a patterned substrate can also be a choice to obtain an ordered NW array. For instance, **Figure 5b** shows single-crystalline perovskite NW

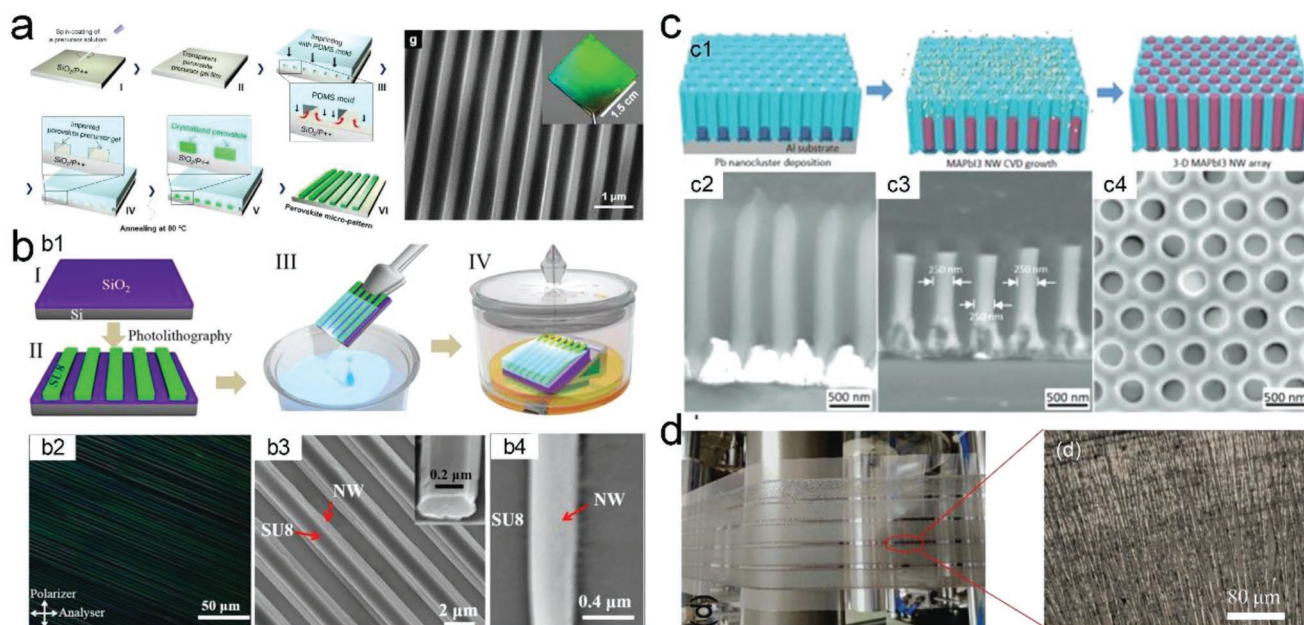


**Figure 5.** Ordered patterns/templates-assisted alignment for MHP NWs arrays. a) PDMS mold-assisted crystallization and alignment: schematic illustration of the fabrication process (left), and SEM image of the well-aligned MAPbBr<sub>3</sub> NW arrays with 400 nm in width (right). The inset is a photograph of the chip showing the light interference pattern. Reproduced with permission.<sup>[136]</sup> Copyright 2016, American Chemical Society. b) Fluid-guided antisolvent vapor-assisted crystallization (FGAVC) method: schematic illustration of the fabrication process (b1), cross-polarized optical image of the MAPbI<sub>3</sub> NW array (b2), and SEM images of the fabricated MHP NW arrays under low (b3) and high (b4) magnification. Reproduced with permission.<sup>[143]</sup> Copyright 2017, American Chemical Society. c) VSSR in highly ordered AAO template for vertically aligned MHP NW arrays fabrication: schematic illustration of the growth process (c1), cross-sectional SEM images of Pb nanoclusters (c2), vertically aligned MAPbI<sub>3</sub> NW arrays (c3), and top-view SEM image of the highly ordered MAPbI<sub>3</sub> NW arrays in AAO template (c4). Reproduced with permission.<sup>[32]</sup> Copyright 2016, John Wiley and Sons. d) R2R microgravure printing method: a photo of the R2R printing process for producing perovskite thin films with highly oriented, large-area PNWs (left) and optical microscopy image of the fabricated MAPbI<sub>3</sub> NWs (right). Reproduced with permission.<sup>[145]</sup> Copyright 2009, Royal Society of Chemistry.

arrays fabricated by a fluid-guided antisolvent vapor-assisted crystallization on the SiO<sub>2</sub>/Si substrate with photoresistor stripes.<sup>[143]</sup> The periodically aligned stripes, which were fabricated by photolithography, helped the precursor solution to form the wire pattern and develop into perovskite NW arrays afterward. The large-area perovskite NW arrays can be observed from the cross-polarized optical image (Figure 5b2) and SEM images (Figure 5b3,b4). Similarly, Pan et al. demonstrated the polystyrene (PS) latex nanoparticles-based nanochannels to fabricate perovskite NW arrays.<sup>[144]</sup> Specifically, a blade coating process was utilized on the substrate with PS particles in aqueous suspensions. The competition between the stress enhancement owing to the loss of residual water from the formed PS nanoparticle film and the stress relaxation through nanoscale crack opening led to the formation of a PS colloidal thin film with periodic nanochannel-like cracks. Subsequently, a highly effective capillary-assisted solution printing process was carried out to fabricate perovskite NWs in the nanochannels. In the final step, the PS stripes were easily removed by toluene, leaving behind aligned perovskite NW arrays on the substrate.

Moreover, Gu et al. used a highly ordered AAO template to grow the vertically aligned perovskite NW arrays.<sup>[32]</sup> They reported for the first time a VSSR process to grow ordered 3D MAPbI<sub>3</sub> NW arrays in a nanoengineered template. Pb nanoclusters were deposited at the bottom of the channel in the beginning, as shown in Figure 5c1,c2. Figure 5c3,c4 shows the cross-sectional and top-view SEM images of MAPbI<sub>3</sub> NW arrays

in the highly ordered AAO template with a high filling ratio and uniformity. Meanwhile, toward future practical applications of MHP NW arrays in electronic and optoelectronic devices, it is significantly meaningful to fabricate large-area and highly ordered MHP NW arrays. Hence, R2R technique has been demonstrated to fabricate highly ordered and ultralong MHP NW arrays.<sup>[145,146]</sup> For example, Hu et al. fabricated ultralong MAPbI<sub>3</sub> NW arrays by large-scale R2R microgravure printing in ambient environments (humidity ≈45%, temperature ≈28 °C), which produced perovskite NW arrays with lengths as long as 15 mm, as shown in Figure 5d.<sup>[145]</sup> Lee et al. demonstrated a PDMS-wrapped cylindrical metal roller that had a periodic array of wide and shallow channels (10 mm wide and 200 nm deep) with narrow spaces (400 nm wide) between the channels for the R2R process.<sup>[146]</sup>

### 3.2. Surface-Guided Alignment

Different from the physical or geometrical confinement of the crystallization discussed above, horizontally aligned MHP NW arrays have also been fabricated on an asymmetric-wettability topographical substrate, as shown in Figure 6a.<sup>[147]</sup> The Si micropillar array had hydrophilic tops and hydrophobic sidewalls, enabling the capillary difference. After dropping the perovskite precursor solution and covering a piece of Si/SiO<sub>2</sub> substrate onto the micropillar array, the solution flow



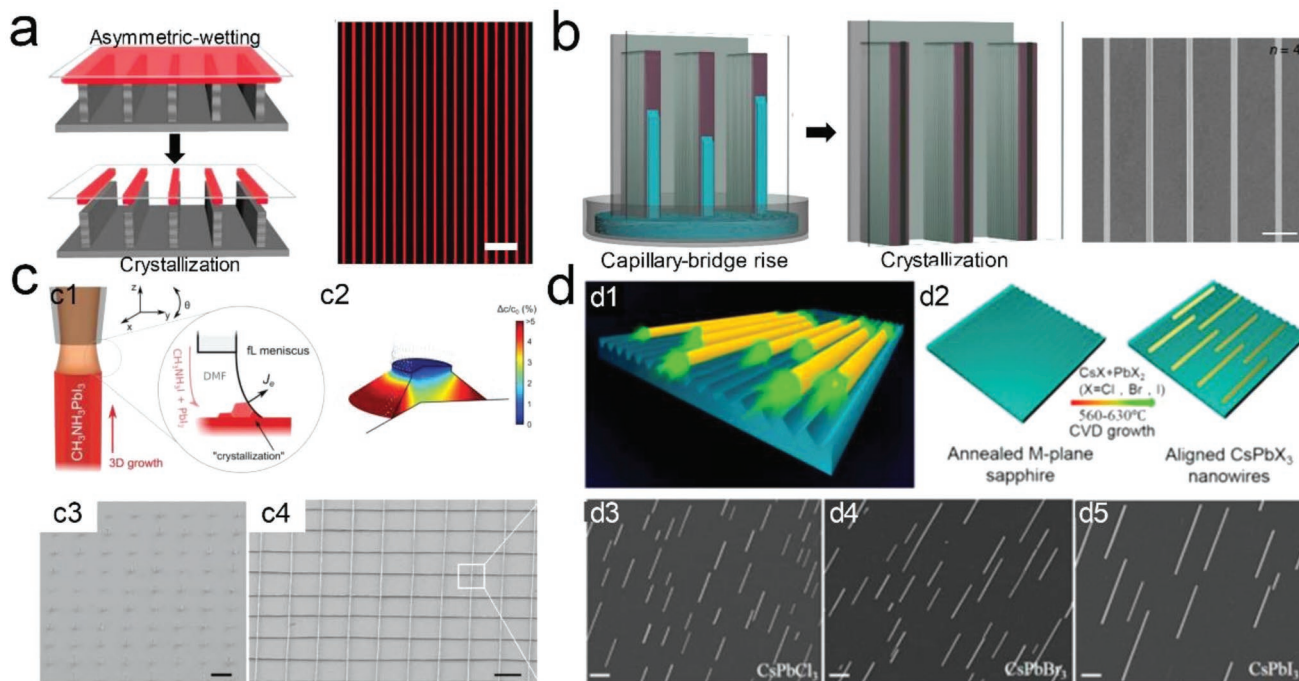


**Figure 6.** Surface-guided alignment for MHP NW arrays. a) Asymmetric-wettability topographical template-assisted crystallization and alignment: schematic illustration of the fabrication process (left), and fluorescent microscope image of the grown  $\alpha$ -CsPbI<sub>3</sub> NW arrays (right). Reproduced with permission.<sup>[147]</sup> Copyright 2019, John Wiley and Sons. b) Capillary bridge rise for crystallization and alignment: schematic illustration of two critical steps for the 2D MHP NW arrays fabrication (left: capillary-bridge rise, middle: dewetting and crystallization), and SEM image of the fabricated  $n = 4$  MHP nanowire arrays (right). Reproduced with permission.<sup>[82]</sup> Copyright 2018, Springer Nature Limited. c) 3D printing method: SEM images of the 3D printed vertically aligned (left) and horizontally aligned (right) MHP NW arrays. Reproduced with permission.<sup>[151]</sup> Copyright 2019, John Wiley and Sons. d) Substrate-guided CVD growth of in-plane aligned MHP NW arrays: schematic of the perovskite NW lasers on an annealed M-plane sapphire substrate (d1), diagram illustration of the growth process (d2), and SEM images for as-grown in-plane aligned CsPbCl<sub>3</sub> (d3), CsPbBr<sub>3</sub> (d4), and CsPbI<sub>3</sub> (d5) NWs. Reproduced with permission.<sup>[152]</sup> Copyright 2018, American Chemical Society.

was confined between the Si micropillar tops and the Si/SiO<sub>2</sub> substrate, forming a sandwich-like self-assembly system. Finally, after the solvent evaporated in a vacuum oven, stable  $\alpha$ -CsPbI<sub>3</sub> NW arrays were obtained with large grain size, high crystallinity, preferential (100) crystallographic orientation, tunable alignment, and long-term stability (>30 days). Subsequently, the same group further revised the asymmetric-wettability Si substrate with rectangle micropillars to fabricate 2D-perovskite ((BA)<sub>2</sub>(MA)<sub>*n*-1</sub>Pb<sub>*n*1</sub>3<sub>*n*+1</sub>, where BA = butylammonium,  $n =$  layer number, 2–5 in this study) NW arrays (Figure 6b).<sup>[82]</sup> Rather than directly dropping the precursor solution onto the micropillars, the sandwich-like system was vertically put into the precursor solution. Thereafter, the capillary force and Laplace pressure drove the perovskite solution to rise inside the gap between Si micropillars and the target substrate, regarded as the capillary-bridge rise assembly system. The obtained single-crystalline 2D NWs were oriented perpendicular to the perovskite layers, and the spatially confined height and width were parallel to the perovskite layer. Similar capillary-assisted MHP perovskite NW arrays fabrication was also reported by others.<sup>[148–150]</sup> Recently, a nanoprecision 3D printing method was developed by Chen et al. for fabricating both horizontally and vertically aligned MHP NW arrays (Figure 6c).<sup>[151]</sup> It was based on guiding evaporation-induced perovskite crystallization process in mid-air, with the utilization of a femtoliter

ink (PbI<sub>2</sub> and MAI in DMF) meniscus formed on a nanopipette. Figure 6c2 shows the calculated concentration field of perovskite solutes inside the meniscus, where a nanosized, rim-shaped high concentration field is formed under solvent evaporation and consequently promotes the nucleation and growth of MAPbI<sub>3</sub> nanocrystals. As one of the most significant advantages over conventional fabrication methods, it enables the fabrication of 3D perovskite crystalline NW arrays with a high degree of controls over NW diameter, direction, position, and even hollowness. Surface-guided epitaxial CVD growth was also reported by Wang et al. for growing high-quality in-plane aligned CsPbX<sub>3</sub> (X = Cl, Br, and I) NW arrays.<sup>[152]</sup> There were ordered V-shaped nanogrooves structures on the annealed M-plane sapphire substrate, resulted from the thermodynamically unstable property of the sapphire, as schematically shown in Figure 6d1. The width and depth of the nanogrooves are  $\approx 80$  and  $\approx 13$  nm, respectively. During the CVD growth, the mixture of CsX and PbX<sub>2</sub> vapors would deposit and nucleate at the nanogrooves due to van der Waals epitaxy, which could serve as seeds to grow into in-plane well-aligned nanowires, as shown in Figure 6d3–d5. More vapor phase growth of well-aligned perovskite NW arrays have also been demonstrated by Tong et al.<sup>[122]</sup> The comparison of typical MHP NWs reviewed above in the aspects of synthesis method, morphology, crystal structure, optical properties, and applications are summarized in Table 1.

**Table 1.** Comparison of different MHP NWs in the aspects of synthesis method, morphology, crystal structure, optical properties, and applications.

Material	Synthesis	Length [ $\mu\text{m}$ ]	Diameter [nm]	Crystal structure	PL peak [nm]	PLQY [%]	Application	Refs.
CsPbBr <sub>3</sub>	Ultrasonication	1–3	12	Orthorhombic	524	10.8	–	Refs. [85]
MAPbBr <sub>3</sub>	Self-assembly	0.3–0.9	3.8	Cubic	524	59	–	[86]
MAPbI <sub>3</sub>	Slip-coating	16	50–200	Cubic	770	–	PD	[87]
MAPbI <sub>3</sub>	Blade-coating	>10 000	2000–3000	Tetragonal	–	–	Image sensor	[31]
MAPbI <sub>3</sub>	Drop-coating	2000	100–2000	Tetragonal	780	–	PD	[84]
CsPbBr <sub>3</sub>	Hot-injection	5	12	Orthorhombic	521	–	–	[70]
CsPbBr <sub>3</sub>	Hot-injection	>1	2.2	Orthorhombic/cubic	465	30	–	[92]
CsPbI <sub>3</sub>	Hot-injection	2	150	Orthorhombic	–	–	PD	[91]
MAPbBr <sub>3</sub>	Extrusion	20	160	Cubic	535	29.5	–	[95]
MAPbI <sub>3</sub>	Spin-coating in AAO	0.425	50–200	Cubic	–	–	–	[96]
MAPbBr <sub>3</sub>	Capillary	0.6–2	150–300	Cubic	525	–	LEDs	[103]
MAPbI <sub>3</sub>	Nanofluid	2	300	–	–	–	PDs	[107]
CsPbBr <sub>3</sub>	VLS	2.78 nm s <sup>-1</sup>	150	Cubic	539	–	PDs/FETs	[110]
MAPbI <sub>3</sub>	VSSR in AAO	2	250	Cubic	790	–	Image sensor	[32]
MAPbBr <sub>3</sub>	CSVr in AAO	≈200	6.4	Cubic	517	92	LEDs	[120]
CsPbBr <sub>3</sub>	CVD	>1000	200–800	Monoclinic	530	–	PDs	[71]
MAPbI <sub>3</sub>	Nanopatterning	>10 000	≈500	–	770	–	LEDs	[128]
(BA) <sub>2</sub> (MA) <sub>n-1</sub> Pb <sub>n</sub> I <sub>3n+1</sub>	Asymmetric-wettability	>1000	2000	2D crystal	730–775	–	PDs	[82]
MAPbI <sub>3</sub>	3D printing	>18	600	Tetragonal	765	–	–	[151]

## 4. Investigation on Material Properties

### 4.1. Materials Stability

Long-term materials stability is one of the core issues plaguing MHPs, that must be solved before the real applications of MHP NWs. Considerable works have used AAO as a mechanically and chemically robust template to grow MHP NWs. Thanks to the self-packaging capability of the nano-engineered template, as-grown MHP NWs can demonstrate an excellent resistance against moisture and oxygen over the thin-film counterpart, as well as better phase stability. For example, Waleed et al. fabricated MASnI<sub>3</sub> NWs in an AAO template with significantly improved moisture stability.<sup>[113]</sup> Different from the MASnI<sub>3</sub> thin-film, where decomposition was a self-sustaining and self-accelerating process (Figure 7a, left), the side walls of AAO could block the lateral diffusion of water and oxygen molecules inside the NWs, resulting in a slower decomposition rate (Figure 7a, middle). The stability test showed that the degradation process of MASnI<sub>3</sub> NWs was slowed down by around 800 times compared with a planar control sample, by monitoring the PL signal decaying (Figure 7a, right). Compared to MAPbI<sub>3</sub>, FAPbI<sub>3</sub> has an elevated decomposition temperature and a slower decomposition process. However, the excellent optoelectronic properties only exist in the cubic black ( $\alpha$ ) phase that will spontaneously transform into an undesired nonperovskite yellow ( $\delta$ ) phase below 150 °C, with much poorer optoelectronic properties.<sup>[153]</sup> Under such consideration, Gu et al. studied the phase stability of FAPbI<sub>3</sub> NWs in AAO templates.<sup>[114]</sup> It was reported that, without further treatment, the template could stabilize

the  $\alpha$  phase of FAPbI<sub>3</sub> NWs for over 7 months under ambient conditions (Figure 7b1) and 8 days in an extreme environment with relative humidity of 97% (Figure 7b2). Such excellent phase stability was attributed to a combinational effect of inhibited *ab* lattice plane expansion (Figure 7b3,b4) and effective blockage of the diffusion of water and oxygen molecules within the templates.

### 4.2. Optical Properties

#### 4.2.1. Lasing Effect

Besides the enhanced stabilities, perovskite NWs have superior optical properties. For example, working as a perfect cavity for Fabry–Pérot resonance, perovskite NWs can work as excellent lasers with high quality factors (*Q*). Zhu et al. demonstrated room-temperature and wavelength-tunable laser from the single-crystalline perovskite NWs with a typical length of ≈20  $\mu\text{m}$ , a width of a few hundred nanometers, and flat rectangular end facets (Figure 8a).<sup>[34]</sup> It had a very low threshold ( $P_{\text{Th}} \approx 220 \text{ nJ cm}^{-2}$ ) and high *Q* value of ≈3600. When operating above  $P_{\text{Th}}$ , the emission mainly came from the two facets of the NW with coherent interference. The modes in the rectangular NW were hybrid, and the fundamental mode was mostly transverse-electric-like (major  $E_x$  and weak  $E_z$ ). The lasing operation was observed at room temperature from most NWs of mixed stoichiometry, covering the near-infrared to the visible range (Figure 8f). More MHP NWs-based lasers have also been reported by other groups with high performance.<sup>[112,124,137,152,154–160]</sup>

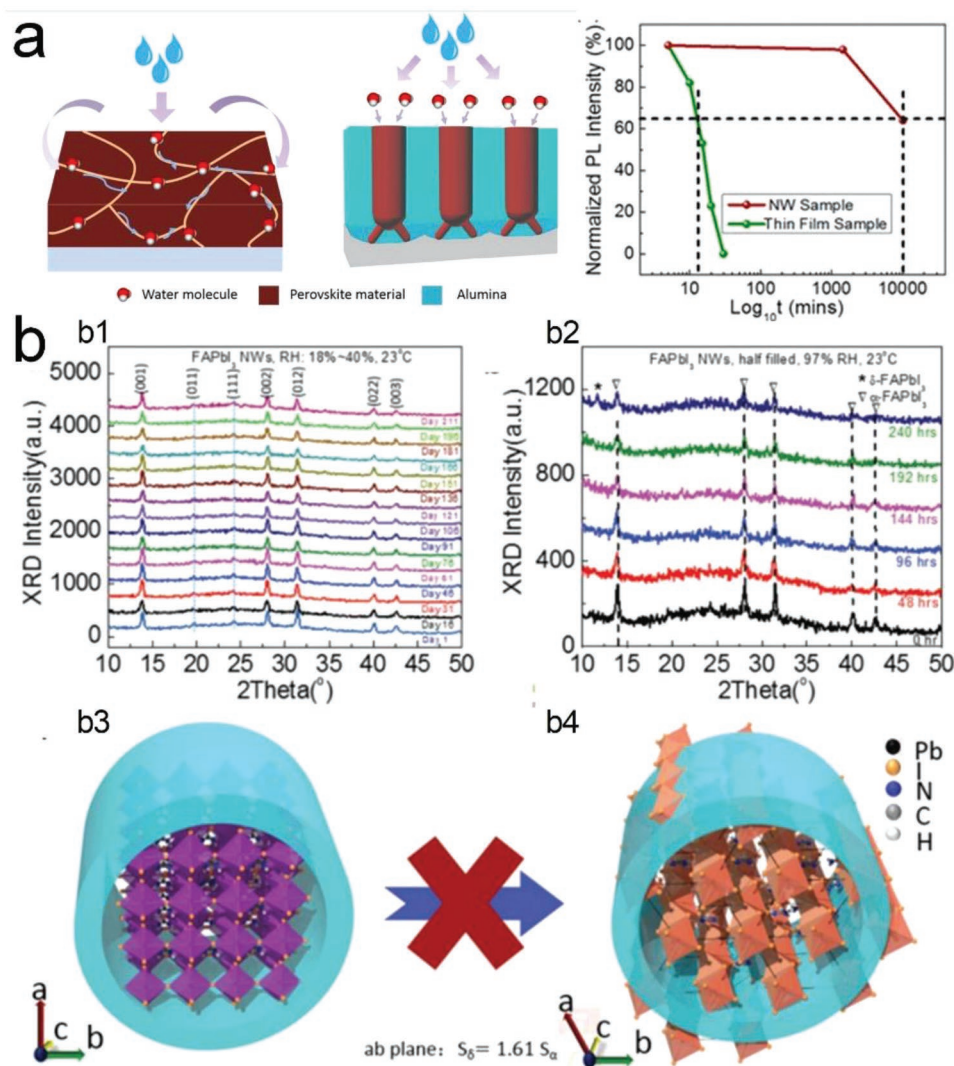


**Figure 7.** Property characterization of MHP NWs: stability. a) Humidity stability: schematic illustration of the MASnI<sub>3</sub> thin film (left) and NWs in AAO template (middle) decay from moisture, and normalized PL emission decay from MASnI<sub>3</sub> thin film and NW samples against logarithmic time scale (right). Reproduced with permission.<sup>[113]</sup> Copyright 2017, American Chemical Society. b) Phase stability: XRD of FAPbI<sub>3</sub> NWs in the freestanding AAO stored under ambient (b1) and wet (b2) conditions versus time, and schematic illustration of the prohibited  $\alpha$  (b3) to  $\delta$  (b4) phase transition of FAPbI<sub>3</sub> NWs through spatial confinement. Reproduced with permission.<sup>[114]</sup> Copyright 2018, Royal Society of Chemistry.

#### 4.2.2. Light and Carrier Propagation

The enhanced resonance in perovskite NWs can be used not only in laser but also in LED, as reported by Fan and co-workers previously (Figure 9a).<sup>[161]</sup> It was demonstrated that horizontally aligned MHP NWs had 50.9% light extraction efficiency, with a 2.9-fold increase over the planar counterpart. It was induced by NWs antenna effect, resulting in a resonance peak of 530 nm, for NWs with diameters of 300, 500, and 550 nm, respectively. Furthermore, perovskite NWs can also show polarization preferences, as reported by Zhou et al. (Figure 9b).<sup>[83]</sup> The Fourier patterns of horizontally printed nanocomposite (perovskite-block copolymer) wire are shown in Figure 9b, left, where a symmetric pattern oriented along the left-to-right axis with two bright lobes at the top and bottom of the image can be observed. It indicates that most dipole contributions are hori-

zontally aligned along the printing axis. For comparison, the Fourier image from a vertical NW (Figure 9b, middle) presents a symmetric pattern about  $\varphi$ , indicative of mostly vertically oriented dipoles. A high emission polarization ratio of  $0.71 \pm 0.03$  can be achieved using a pair of polarizers, one in the excitation path and the other in the emission path (Figure 9b, right). Shang et al. studied the light propagation in the CsPbBr<sub>3</sub> NWs (Figure 9c).<sup>[162]</sup> Owing to strong exciton–photon interactions, the light was guided as an exciton–polariton inside the NWs at room temperature. It was found that both the real ( $n_{||}$ ) and imaginary ( $k_{||}$ ) parts of the refractive index increased dramatically when approaching exciton resonance ( $E - E_0 \approx 0$ ), thus slowing light and enhancing absorption, respectively. Meanwhile, reducing the NWs dimension increased the exciton–photon coupling and the exciton fraction, which would consequently increase the light absorption coefficient and group

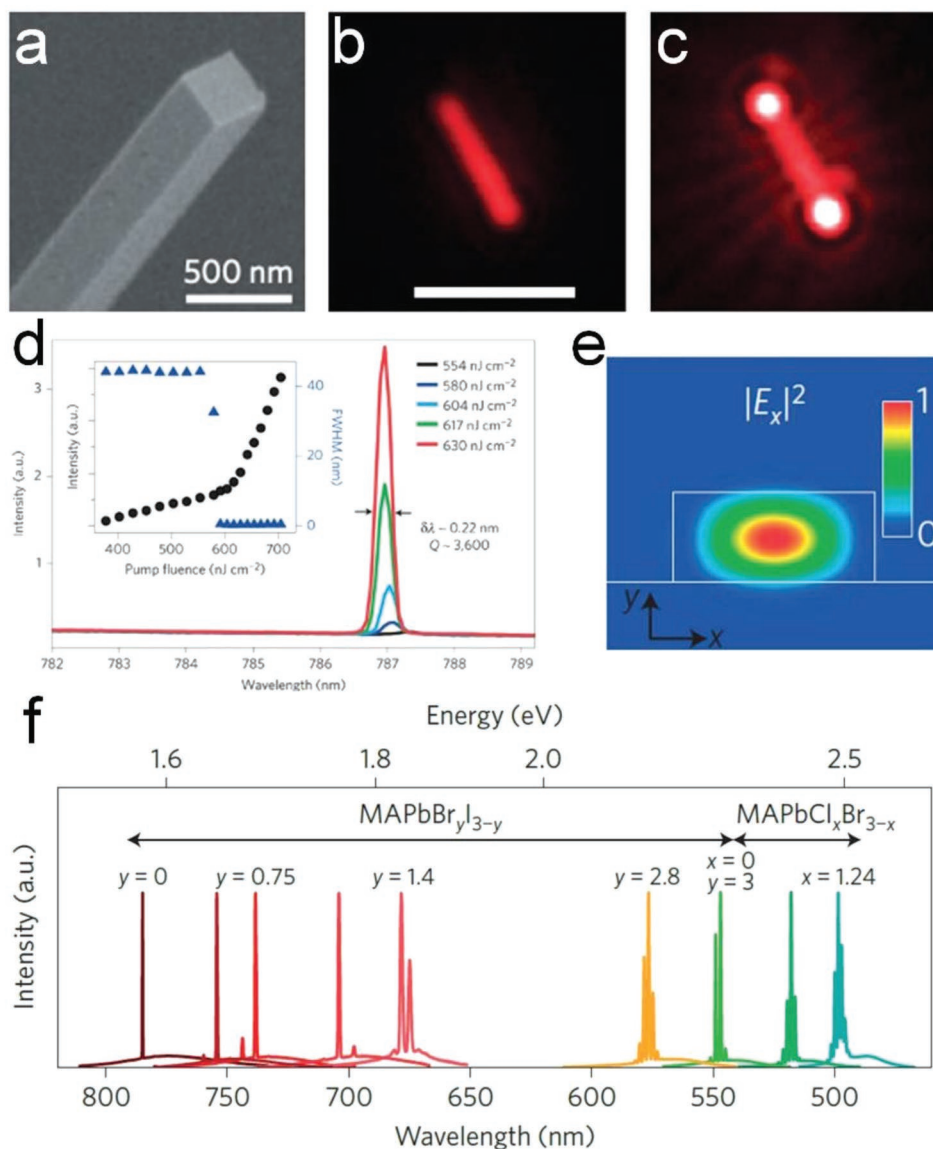


**Figure 8.** Property characterization of MHP NWs: lasing effect. MAPbI<sub>3</sub> NWs for lasing: a) SEM image of a single MAPbI<sub>3</sub> NW showing a square or rectangular cross-section and flat end facets perpendicular to the long NW axis, b) fluorescence images of the NW emission below, and c) above  $P_{Th}$ , d) NW emission spectra around the lasing threshold, and e) cross-sectional view of the simulated electric field intensity profiles at 790 nm for fundamental waveguide modes in a MAPbI<sub>3</sub> NW (width = 600 nm, height = 300 nm) on a SiO<sub>2</sub>/Si substrate, f) widely tunable lasing emission wavelength at room temperature from single-crystal NW lasers of mixed lead halide perovskites. Reproduced with permission.<sup>[34]</sup> Copyright 2015, Springer Nature Limited.

index five- and threefold, respectively. And it also slowed the light group velocity by  $\approx 74\%$ . In addition to the light propagation, photogenerated carrier propagation is also of equal importance for a better understanding of the energy transport mechanism perovskite NWs. Under such consideration, Oksenberg et al. provided a comprehensive study on the propagation of photo-generated electrons and holes in a single CsPbBr<sub>3</sub> NW, with the utilization of experimental data and a proposed model.<sup>[163]</sup> As shown in Figure 9d, top, time-resolved PL (TRPL), employing the time-corrected single-photon counting method, was studied at different locations within a single CsPbBr<sub>3</sub> NW. Much slower kinetics was observed at the end of the NW where it was 15  $\mu\text{m}$  away from the excitation spot (Figure 9d, middle). PL decays

were measured at more locations, as shown in Figure 9d, bottom. It was very obvious that the TRPL decay assumed an unconventional shape with a normal decay at early time and a hump at later time. By modeling the PL signal delay, such a PL signal decay described the time it took for carriers initially generated at the illumination point to diffuse to the detection point before recombining to generate a PL signal. An ambipolar carrier mobility ( $\mu = 35 \text{ cm}^2 \text{ V}^{-1} \text{ s}^{-1}$ ) was further determined with the developed model. Hence, the photon recycling to the total energy transport is negligible compared to charge carrier diffusion for CsPbBr<sub>3</sub> NWs. There is no doubt that clarifying the light-matter interaction in MHP NWs is of significant importance to improve their optoelectronic device performance.

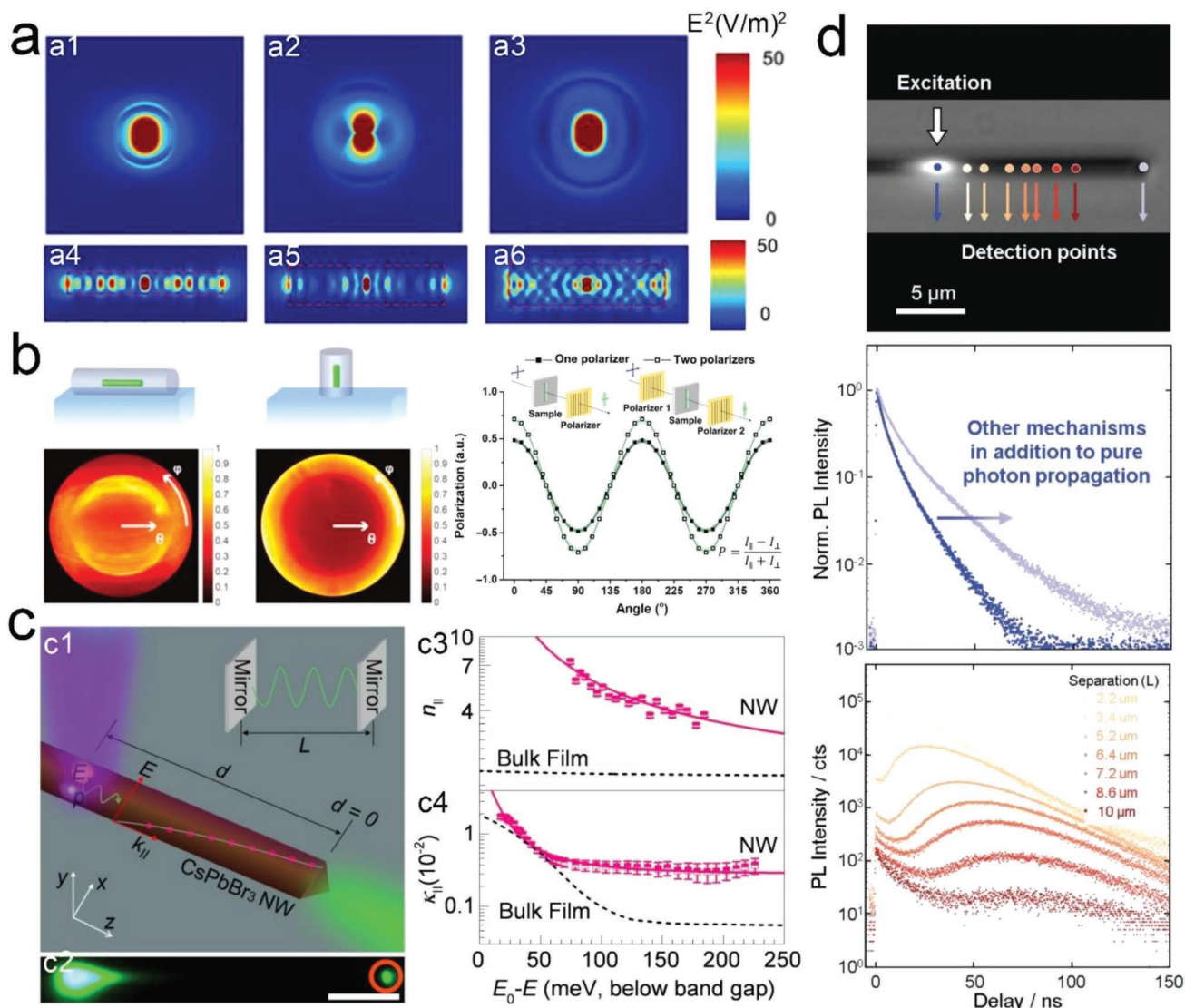


**Figure 9.** Property characterization of MHP NWs: light and carrier propagation. a) Resonance emission enhancement: radial-plane (a1–a3) and axial-plane (a4–a6) cross-sectional  $E^2$  profiles of the MHP NWs with diameters of 300 nm (a1,a4), 500 nm (a2,a5), and 550 nm (a3,a6). Reproduced with permission.<sup>[161]</sup> Copyright 2021, IEEE. b) Polarized emission preference: Fourier images showing the angular emission from a nanowire bundle on the printed horizontal (left) and a vertical (middle) filament on a glass slide, and the polarized emission of printed nanowire composites (right). Reproduced with permission.<sup>[83]</sup> Copyright 2019, American Association for the Advancement of Science. c) Light propagation: (c1) Schematic diagram of light propagation along a CsPbBr<sub>3</sub> NW, (c2) optical image of a representative NW. Scale bar: 5.0  $\mu\text{m}$ . Energy-dependent refractive index,  $n_{||}$  (real part, c3) and  $k_{||}$  (imaginary part, c4), of perovskite bulk film and NWs. Reproduced with permission.<sup>[162]</sup> Copyright 2020, American Chemical Society. d) Carrier propagation in a single CsPbBr<sub>3</sub> NW: (top) overlaid transmission and PL image of the same NW with labeled excitation and detection spots, (middle) TRPL decays measured at the point of excitation and at the end of the NW, and (bottom) decay curves measured at different positions between the excitation and the end of the NW. Reproduced with permission.<sup>[163]</sup> Copyright 2021, John Wiley and Sons.

## 5. Optoelectronic Applications

### 5.1. Solar Cells

Solar energy is the most abundant form of clean energy in the world. High-performance solar cells must harvest sunlight over a broad range of incident angles and wavelengths to realize sufficient daily energy output. Extensive studies have revealed that the 1D nature of semiconductor NWs can provide excellent electrical, optical, and physical properties compared to

bulk counterparts.<sup>[164]</sup> Further, modifying these properties and optimizing solar cell PCE is achievable by controlling the NWs dimensions.<sup>[165–169]</sup> Under such consideration, MHP NWs have been widely used in solar cells. For instance, Im et al. reported the first MHP NWs-based solar cells, where the NWs with a mean diameter of 100 nm were fabricated by a two-step spin-coating procedure (Figure 10a, left).<sup>[170]</sup> It showed faster carrier separation in the presence of a hole transporting layer and higher lateral conductivity than the 3D nanocuboid crystals, as shown in Figure 10a, middle. The photogenerated carrier

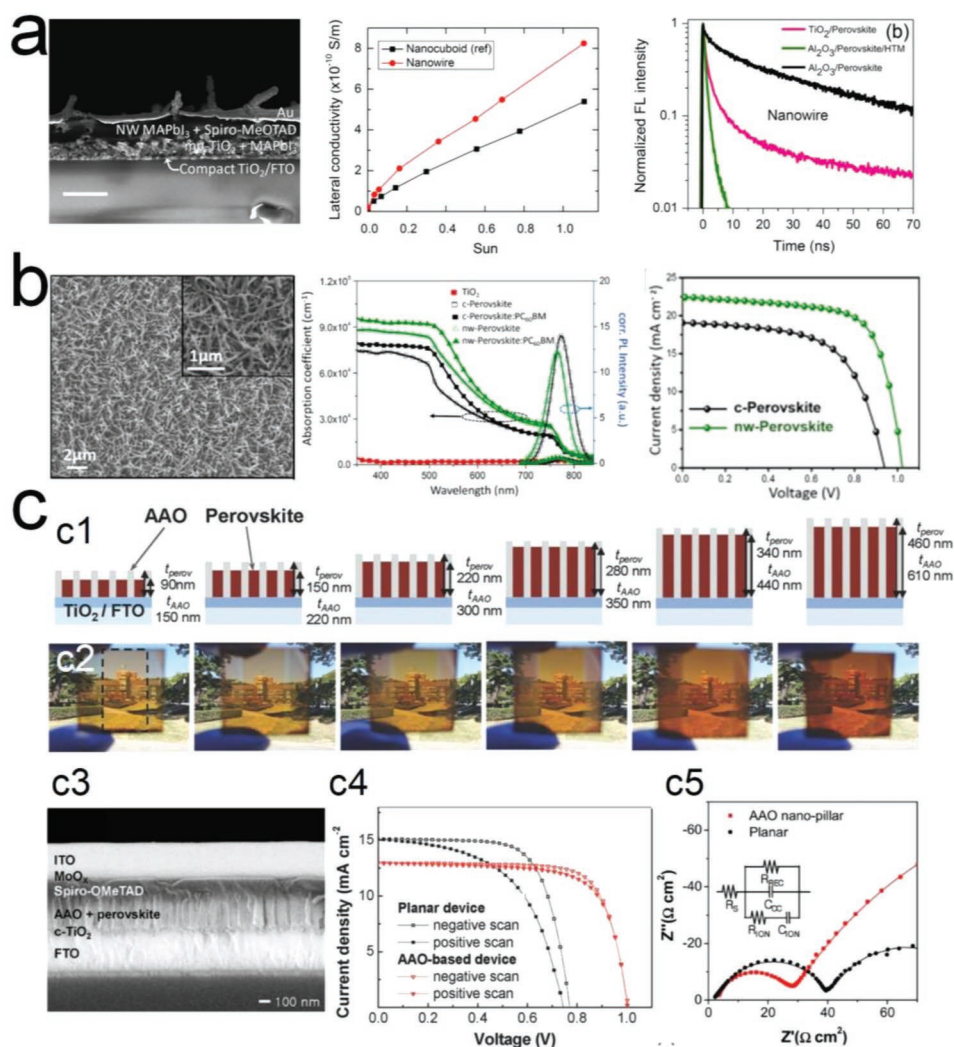


**Figure 10.** MHP NWs for solar cells applications. a) Increased carrier mobility in MHP NWs: cross-sectional SEM images of a full cell employing MAPbI<sub>3</sub> NWs (left). Scale bar represents 1 μm. DC conductivity of the in-plane perovskite by evaporating two gold contacts 0.14 μm apart onto a film (middle), and normalized fluorescence (FL) decay kinetics of different perovskite samples with excitation wavelength of 406 nm (right). Reproduced with permission.<sup>[170]</sup> Copyright 2015, American Chemical Society. b) Enhanced light harvesting in MHP NWs: top-view SEM images of MHP NWs (left), absorption coefficient and PL spectra of the different samples (middle), *J*-*V* characteristics for the highest performing c-perovskite and NW-perovskite (right). Reproduced with permission.<sup>[72]</sup> Copyright 2018, Elsevier Ltd. c) MHP NWs based semitransparent solar cells: Schematic illustration (c1) and corresponding photography (c2) of MHP NWs in AAO templates with different thicknesses (prepared without Au cathode). The dotted line in the first picture indicates the area where the AAO template exists (active area). (c3) Cross-sectional SEM image of a completed device, (c4) *J*-*V* curves and (c5) Nyquist plots for the planar and NWs-based devices. Reproduced with permission.<sup>[101]</sup> Copyright 2016, John Wiley and Sons.

collection plays a critical role in impacting the performance of solar cells, in terms of short-circuit current density (*J*<sub>sc</sub>) and fill factor (FF). As a result, the best performing device employing MAPbI<sub>3</sub> NWs delivered a PCE of 14.71% (*J*<sub>sc</sub> = 19.12 mA cm<sup>-2</sup>, open-circuit voltage (*V*<sub>oc</sub>) = 1.052 V, FF = 0.721).

Another appealing feature of MHP NWs is the light-trapping enhanced absorption. Singh et al. also reported excellent photovoltaic performance in MHP NWs-based solar cells (Figure 10b).<sup>[72]</sup> The optimal perovskite NWs exhibited enhanced absorption in the visible region, improved charge separation, and high charge carrier mobility, compared to the thin film counterpart (Figure 10b, middle). Consequently, the device reached a champion PCE of 18.7% (Figure 10b, right). Notably, the size confinement effect allows a long absorption

path along the long wire, thereby contributing to much higher *J*<sub>sc</sub> than compact films. Kwon et al. demonstrated semitransparent MHP NWs-based solar cells by utilizing AAO as a scaffolding layer.<sup>[101]</sup> As shown in Figure 10c1,c2, the transparency could be precisely controlled by varying the AAO pore size and height. In Figure 10c3,c4, after modifying the nanostructured device's geometry, a high-performance semitransparent solar cell was achieved with a PCE value of 9.6% and a whole device average visible light transmittance of 33.4%. It is noteworthy that the internal ion diffusion was remarkably suppressed in perovskite NWs due to the AAO scaffold (Figure 10c5), which significantly improved light-soaking stability and resulted in negligible hysteresis behavior. To address the stability issue, Liao et al. fabricated all-inorganic perovskite (CsPbI<sub>3</sub> and

CsPbBr<sub>3</sub>) NWs-based solar cells.<sup>[171]</sup> When the perovskite NWs-based device was stored in a dark ambient environment, an impressive lifetime of 5500 h was achieved (remains 99% of the initial PCE). Raja et al. proposed a new design for multijunction solar cells to obtain high PCEs.<sup>[172]</sup> The design was based on the integration of MHP NW arrays on a Ge substrate, providing descending order bandgaps from the perovskite (1.6 eV) to the Ge substrate (0.7 eV). It would reduce the energy losses due to the thermalization effect. The calculation revealed that the geometrically optimized NWs with a diameter of 105 nm possessed a remarkable current density of 20.3 mA cm<sup>-2</sup>. More MHP NWs-based solar cells have also been demonstrated by other groups.<sup>[173,174]</sup>

## 5.2. Photodetectors

Compared with thin-film counterparts, semiconductor NWs are well known to have additional advantages in PD applications, such as improved light trapping, fewer grain boundaries, lower defect density, longer photocarrier lifetime, better mechanical properties, which are essential for flexible devices, to name but a few.<sup>[79,80,175–179]</sup> MHP NWs-based PD devices have also been numerous fabricated and studied, demonstrating excellent performance.

Horváth et al., for the first time, reported the slip-coating assisted synthesis of 2 sets of MAPbI<sub>3</sub> NWs with mean diameters of 50 and 400 nm and lengths up to 10 μm, and further applied them in the PD applications, as shown in Figure 11a,

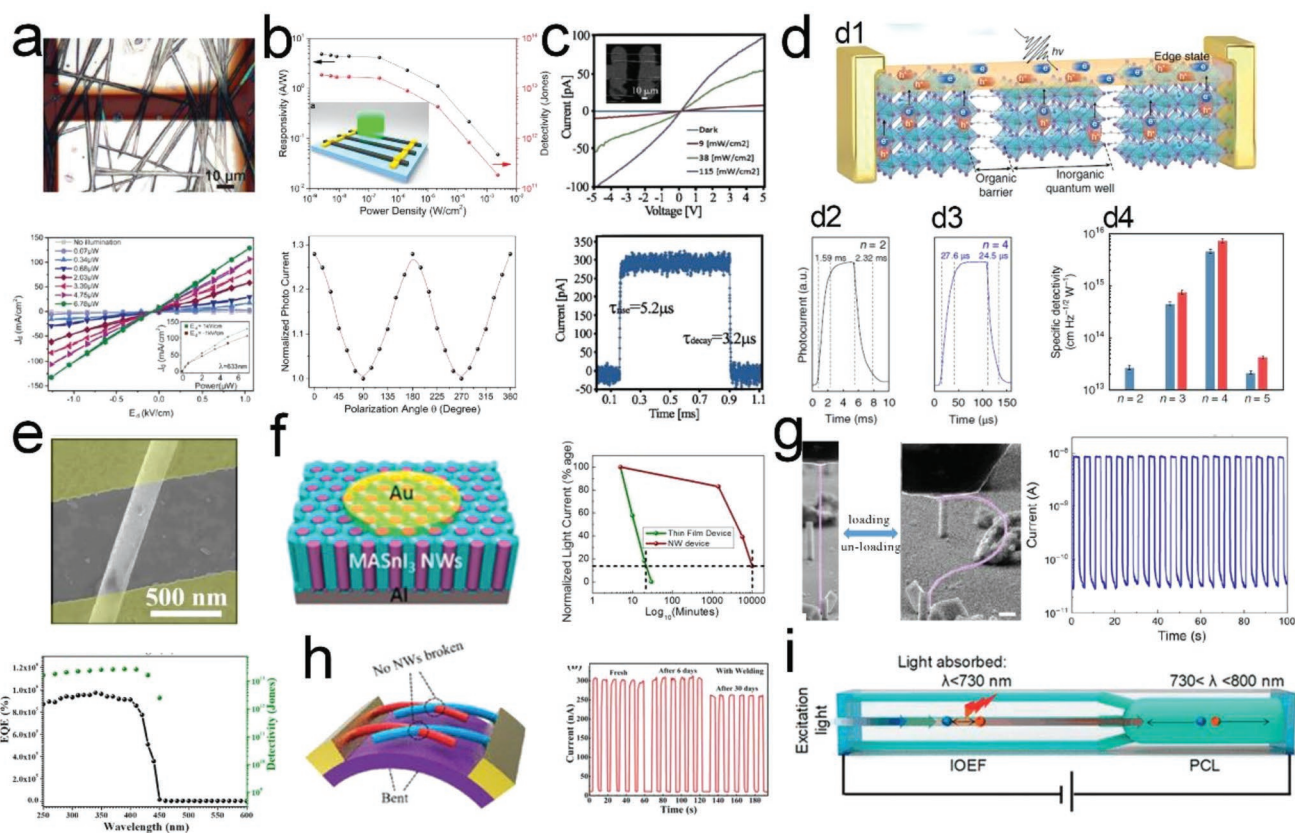


**Figure 11.** MHP NWs for PD applications. a) Random MAPbI<sub>3</sub> NWs-based PD: optical microscopy image of the device (top) and *I*–*V* curves under different laser illumination power conditions (bottom). Reproduced with permission.<sup>[87]</sup> Copyright 2014, American Chemical Society. b) MAPbI<sub>3</sub> NWs-based PD device with high detectivity and polarization sensitivity: light intensity-dependent responsivity and detectivity (top), and normalized photocurrent of the device as a function of the polarization angle  $\theta$  (bottom). Reproduced with permission.<sup>[84]</sup> Copyright 2016, American Chemical Society. c) CsPbBr<sub>3</sub> NWs-based PD device with ultrafast response speed: *I*–*V* curves under different laser illumination power conditions (top) and a single cycle of on–off switching showing 5.2 and 3.2 μs response time (bottom). Reproduced with permission.<sup>[181]</sup> Copyright 2017, American Chemical Society. d) Layered MHP NWs for ultrasensitive PD: schematic illustration of the device (d1), the temporal response of 1D arrays of layered MHP with *n* = 2 (d2) and 4 (d3), and statistics of device detectivities with *n* = 2–5 NWs (d4). Reproduced with permission.<sup>[82]</sup> Copyright 2018, Springer Nature Limited. e) Single CsPbI<sub>3</sub> NW-based PD with ultrahigh EQE and detectivity: representative SEM image of the device (top), and approximate EQE and detectivity of the device at different wavelengths (bottom). Reproduced with permission.<sup>[91]</sup> Copyright 2018, American Chemical Society. f) Stable MASnI<sub>3</sub> NWs-based PD device: schematic illustration of the device (left), and normalized light current decay from thin film and NW devices against logarithmic time scale (right). Reproduced with permission.<sup>[113]</sup> Copyright 2017, American Chemical Society. g) Single CsPbBr<sub>3</sub> NW-based PD with good flexibility: SEM images of the original geometry (left) and the maximum elastic deformation (middle) of a single CsPbBr<sub>3</sub> NW, and the device photocurrent under on/off switching light illumination (0.2 Hz) as a function of time after 5000 bending cycles (right). Reproduced with permission.<sup>[182]</sup> Copyright 2021, Springer Nature Limited. h) Welding MAPbI<sub>3</sub> NWs for stable and flexible PD: schematic illustration of the bent device (left), and *I*–*t* curves of the device with different storage times (right). Reproduced with permission.<sup>[183]</sup> Copyright 2020, American Chemical Society. i) Schematic illustration of MAPbI<sub>3</sub> QW/NW arrays based narrowband PDs. Reproduced with permission.<sup>[184]</sup> Copyright 2022, American Chemical Society.

top.<sup>[87]</sup> In the dark state, the device behaved like a good insulator with a current value in the order of tens of pA and resistances in the GΩ range (Figure 11a, bottom). The lowest detection light power could reach 70 nW. Meanwhile, the device showed less than 500 μs response time under the on–off light illumination, which was  $\approx 10^4$  faster than the state-of-the-art PDs made of monolayer MoS<sub>2</sub> and graphene at that time. They also reported the combination of the microengineered MAPbI<sub>3</sub> NW and graphene for low intensity (pW) light detection with ultra-high responsivity ( $2.6 \times 10^6$  A W<sup>-1</sup>) at room temperature.<sup>[81]</sup> The drastic enhancement of such detection performance could be mainly attributed to the NW morphology.

Considering the morphological anisotropy property emanating from the 1D structure, MHP NWs-based photodetector was also, for the first time, reported to show the polarization sensitivity by Gao et al. (Figure 11b).<sup>[84]</sup> The device showed maximum responsivity of 4.95 A W<sup>-1</sup> and detectivity of  $2 \times 10^{13}$  Jones at an excitation light intensity of  $\approx 2.5$  nW cm<sup>-2</sup>, as illustrated in Figure 11b, top. More importantly, the NWs-based PD device showed peaks and valleys of photocurrents at the angles where the light was polarized in parallel and perpendicular to the NW orientation axis, respectively (Figure 11b, bottom). The peak-to-valley ratio of 1.3 proved the intense polarization-dependent detection of the NWs-based PD device. Similar polarized light detection with the utilization of 2D MHP NWs was reported by Ghoshal et al., where a record high photocurrent anisotropy ratio of  $\approx 3.62$  was achieved.<sup>[180]</sup>

Oksenberg et al. reported horizontally aligned CsPbBr<sub>3</sub> NWs with a uniform crystallographic orientation on flat and faceted sapphire surfaces.<sup>[181]</sup> The NWs diameter could be tuned from 2 μm down to 20 nm, with the quantum confinement effect-induced PL emission shift. As shown in Figure 11c, bottom, the NWs-based photodetectors on M-plane sapphire substrate showed ultrafast response speed (5.2/3.2 μs), which was faster than any other CsPbBr<sub>3</sub>-based PD devices. Such a high performance could be attributed to the high quality, single-crystalline, and grain boundary-free nature of the obtained NWs. Feng et al. reported a single-crystalline layered perovskite NWs-based ultrasensitive PDs.<sup>[82]</sup> The scheme of carrier dynamics in the device is shown in Figure 11d1. This device configuration integrates insulating organic barriers in a carrier-transport pathway for suppressing the dark current (<1 pA). Meanwhile, provided by the exposed crystalline edges, a highly photoconductive channel in the device is very efficient in exciton dissociation, free-carrier conduction, and charge injection. Consequently, high average responsivities of  $1.5 \times 10^4$  A W<sup>-1</sup>, detectivities of more than  $7 \times 10^{15}$  Jones and response time of  $\approx 25$  μs have been achieved on a single device based on  $n = 4$  2D perovskite NWs (Figure 11d2–d4). In addition, a single inorganic perovskite (CsPbI<sub>3</sub>) NW-based PD device was reported by Yang et al. to possess a responsivity of  $2.92 \times 10^3$  A W<sup>-1</sup>, detectivity of  $5.17 \times 10^{13}$  Jones, EQE of  $5 \times 10^9\%$ , and an ultrafast response time of 50 μs (Figure 11e).<sup>[91]</sup> It is noted that the detectivity value was more than five times of the best one ever reported at that moment. Waleed et al. reported the vertically aligned lead-free perovskite (MASnI<sub>3</sub>) NW arrays embedded in AAO templates for stable photodetectors (Figure 11f, left).<sup>[113]</sup> Since those NWs were embedded in mechanically and chemically robust templates, the MASnI<sub>3</sub> decay process has been dramatically slowed

down by up to 840 times, as compared with a planar thin-film, as discussed in Section 3. Consequently, the NWs-based photodetectors were demonstrated to have a 500 times slower photocurrent decay than the thin-film devices (Figure 11f, right). It provided a promising scheme for achieving stable MHP-based high performance PD devices.

As another obvious advantage of MHP NWs, the compatibility of flexible devices is significantly attractive for wearable optoelectronics. For instance, Li et al. demonstrated high flexural elasticity (an elastic strain of  $\approx 4\%$  to 5.1%) of a vertical CsPbBr<sub>3</sub> NW, as shown in Figure 11g, left and middle.<sup>[182]</sup> Thereafter, in a single NW-based flexible PD device, there was no noticeable performance deterioration observed after 5000 bending cycles (Figure 11g, right). However, in most NW-based devices, the existence of microinterfaces between NWs seriously hindered the radial transmission of the photogenerated carriers, which would impede the device performance to a certain degree. Meanwhile, suffering from the unbalanced tension, the stacked structure of NWs would easily lead to partial fracture of the upper layer of NWs during the bending process. The device flexibility was consequently limited. To overcome such a problem, Wu et al. fabricated flexible PD devices based on welded perovskite NWs with excellent flexibility, as schematically shown in Figure 11h, left.<sup>[183]</sup> In such a unique NWs network structure, all NWs formed a film without stacking and hence the microinterfaces were greatly reduced. The fabricated PD device showed not only excellent stability but also flexibility. Specifically, the photocurrent was decreased by more than 60% and less than 1% after 250 cycles of bending at the smallest bending radii, for devices without and with NWs welding, respectively (Figure 11h, right). Recently, Zhang et al., for the first time, demonstrated MAPbI<sub>3</sub> QW/NW arrays-based narrowband PDs with a certain flexibility, as shown in Figure 11i.<sup>[184]</sup> Two cutoff detection edges of the NPDs are located at  $\approx 770$  and 730 nm, with a full width at half-maxima of  $\approx 40$  nm. The optical bandgap difference between the NWs and the QWs, in conjunction with the high carrier recombination rate in QWs, contributes to the intriguing narrowband photodetection performance. It provided a new pathway to design and engineer a nanostructured MHP for novel color selective and full color sensing devices. More MHP NWs-based flexible PD devices with good performance have also been reported by others.<sup>[107,185–191]</sup> The excellent mechanical reliability suggests great potential of MHP NWs in flexible/wearable electronics when integrated with various flexible transparent electrodes, such as Ag NWs,<sup>[192]</sup> or inkjet printed inorganic conductive materials.<sup>[193,194]</sup>

In addition to detection of visible photon, NHP NWs have also been utilized for X-ray photon detection. For example, Zhang et al. fabricated 15-μm-long single-crystalline CsPbBr<sub>3</sub> NWs in AAO templates and applied them as X-ray scintillators.<sup>[102]</sup> A maximum photon yield of  $\approx 5300$  ph MeV<sup>-1</sup> was obtained for NWs with a diameter of 30 nm. Benefiting from the physical confinement of AAO, the scintillators showed high resistance to continuous X-ray radiation and ambient condition storage, where only 20–30% scintillation-intensity decrease was observed after 24 h X-ray exposure. Meanwhile, X-ray imaging with  $\approx 2$  μm spatial resolution was demonstrated. Kundu et al. reported solution-grown  $\delta$ -CsPbI<sub>3</sub> microwires for X-ray detection with high performance.<sup>[195]</sup> Specifically, the ITO/ $\delta$ -CsPbI<sub>3</sub>



microwires/ITO device exhibited one of the lowest detectable X-ray dose rates at  $33.3 \text{ nGy}_{\text{air}} \text{ s}^{-1}$ , resulted from the exceptionally low dark current density of  $12 \text{ pA mm}^{-2}$ . Meanwhile, the microwires-based X-ray detector demonstrated excellent operational stability under a high continuous X-ray dose rate of  $45 \text{ Gy}_{\text{air}} \text{ s}^{-1}$ . No obvious current decrease was observed after exposure to an accumulated radiation dose of  $1.44 \times 10^6 \text{ Gy}_{\text{air}} \text{ s}^{-1}$ , equivalent to 720 million chest X-rays.

### 5.3. Image Sensors and Bionic Eyes

Image sensors are devices consisting of millions of PD devices, where every single PD device serves as a pixel for imaging. Compared to individual PD devices, image sensors have more comprehensive applications in many fields such as artificial intelligence, medical health, and wearable electronics.<sup>[196]</sup> Several research groups have fabricated MHP nanostructure-based image sensors. In 2016, Jie et al. introduced a low-cost and simple blade coating method for large-area synthesis of  $\text{MAPbI}_3$  microwire arrays, which were horizontally aligned on the substrate.<sup>[31]</sup> By depositing electrodes at the two ends of these microwires, they have achieved PDs with the typical architecture of field-effect transistors (Figure 12a, left). By patterning these electrodes, they have further assembled a flexible  $21 \times 21$ -pixels image sensor on a PET substrate. Under different bending conditions, the flexible image sensor could clearly display letters (Letter “e”) (Figure 12a, middle and right). Considering that the diameter of 1D nano/microstructures is much smaller than their length, the NW density can be greatly improved by aligning them vertically on the substrate. Hence, Fan et al. fabricated this kind of 3D perovskite NW arrays using template-assisted VSSR growth method. The as-prepared ordered 3D perovskite NW arrays could reach an ultrahigh NW density up to  $4 \times 10^8\text{--}10^9 \text{ cm}^{-2}$ .<sup>[32]</sup> Figure 12b1 shows the schematic of a proof-of-concept image sensor, which has a crossbar structure with photodetectors located at the intersection of the top and bottom electrodes. The image sensor could verify the projection recognition of various optical patterns. Letters such as “H”, “C”, and “K” and the heart symbol have been reconstructed to prove its function (Figure 12b2–b5). It is worth noting that although there were only 1024 pixels demonstrated in the device, the pixel number could be actually improved to that of the NWs as they were well isolated by the insulating  $\text{Al}_2\text{O}_3$  template so that each NW could serve as an individual PD pixel.

In 2020, Fan et al. reported a biomimetic eye with a hemispherical NW arrays retina.<sup>[33]</sup> The critical technology was to conform the NW arrays into hemispherical shape and the corresponding back electrodes integration. In combination with the optical system, they achieved a spherical eye, which had paradigm very close to that of the biological human eyes (Figure 12c1,c2). Actually, the spherical structure is one of the main characteristics of the human eyes. It can reduce the aberration, simplify the device structure, and enable a larger field-of-view. However, currently, our manmade cameras cannot achieve this due to the incompatibility between the spherical substrate and the prevalent semiconductor fabrication process. In addition to the retina, the prepared artificial eye completely

mimicked the primary structure of the human eye. The front optical lens, ionic liquid, perovskite NW array, and rear liquid metal fibers corresponded to the crystalline lens, vitreous, rod cells, and nerve fibers of the human eye, respectively. The artificial eyeball exhibited excellent light response characteristics and could reconstruct patterns projected on it (Letter “A”, Figure 12c3). It has also exhibited a wider field-of-view than its planar counterpart (Figure 12c4,c5). The low resolution of the patterns was caused by the low density of liquid metal fibers, which could be significantly improved by incorporating high-precision automatic manipulation equipment in the back electrodes integration process. To further prove the application potential of the prepared artificial visual system in ultrahigh pixel sensing, PDs based on single or several NWs were investigated through the advanced micro- and nanoprocessing technologies and magnetic field-assisted positioning strategy, which showed distinguishably stable photocurrents. The device held great promise in high-resolution imaging, approaching human eyes for spherical biomimetic eyes. Although there were still several problems to address before practical applications, it could inspire scientists to develop more intelligent visual sensors and other bionic electronic devices. The totality of the results in these studies implies that the aligned perovskite NW (MW) arrays hold a great possibility for low-cost, large-scale, and high-efficiency image sensors.

### 5.4. LEDs

Owing to the superior optoelectronic properties, intrinsic to the perovskite NWs, they can be utilized for high-performance LEDs. Wong et al. fabricated the first vertical  $\text{MAPbBr}_3$  NR arrays-based LEDs that consist of ITO/PEDOT:PSS/ $\text{MAPbBr}_3$  NRs/F8/Ca/Ag, as schematically shown in Figure 13a, top.<sup>[197]</sup> The EL image of the microscale device is shown in Figure 13a, bottom, demonstrating strikingly green EL. However, the high current density exceeds  $10 \text{ A cm}^{-2}$ , declined EQE of the device. Fan and co-workers also reported vertical perovskite NW arrays-based LEDs with a 100% NW filling ratio in the AAO template, as demonstrated by the schematic device structure in Figure 13b1.<sup>[103]</sup> The EQE of the LED devices was enhanced to 16% compared to 11% of the planar counterpart (Figure 13b2), which can be attributed to the enhanced light extraction efficiency in perovskite NW devices possessing leaky mode behavior at the emission wavelength. Moreover, the device half-lifetime was also increased from 13 to 37 min, benefiting from the better thermal conductance of alumina and hence reduced the Joule heating in perovskites (Figure 13b3). Intriguingly, the protection from AAO also increased the mechanical robustness of the devices and the NW device. Specifically, the NWs-based device remained 86% electrical luminance when bent to  $180^\circ$  (Figure 13b4). Wu et al. demonstrated a green-white color switchable LED device based on laterally fused  $\text{CsPbBr}_3$  NWs.<sup>[198]</sup> The horizontally aligned perovskite NWs were utilized as the emission layer, as shown in Figure 13c, left. It is interesting that, at high NW concentration, the LED emitted pure-green light, and the carriers transported through Fowler–Nordheim (FN) quantum tunneling and direct injection successively (Figure 13c, middle).

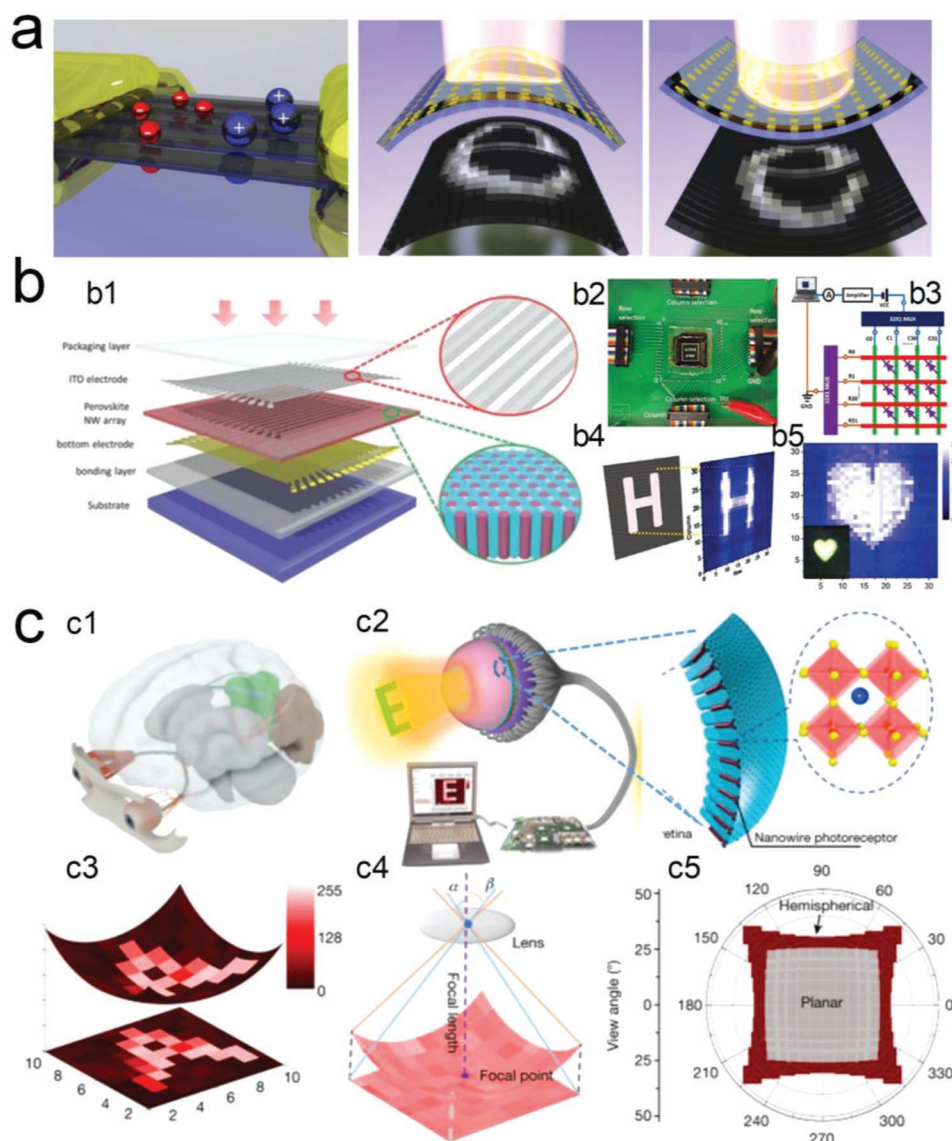


**Figure 12.** MHP NWs for image sensor and bionic eye applications. a) Horizontal MAPbI<sub>3</sub> NWs-based image sensor: schematic illustration of a single PD device (left), image sensing process with different device bending directions (tensile (middle) and compressive (right)). Reproduced with permission.<sup>[31]</sup> Copyright 2016, John Wiley and Sons. b) Vertically aligned MAPbI<sub>3</sub> NW arrays-based image sensor: schematic illustration of the device (b1), a photograph of an image sensor mounted on a printed circuit board (b2), schematic illustration of the measurement setup (b3), original and imaged letter (“H”) (b4), and original and imaged love heart pattern (b5). Reproduced with permission.<sup>[32]</sup> Copyright 2016, John Wiley and Sons. c) Hemispherical FAPbI<sub>3</sub> NW arrays based bionic eyes: schematic illustration of the human eyes (c1) and the NWs based bionic eyes (c2), reconstructed image (letter “A”) of bionic eyes and its projection on a flat plane (c3), schematic (c4) and calculated (c5) FOV of the planar and hemispherical image-sensing systems. Reproduced with permission.<sup>[33]</sup> Copyright 2020, Springer Nature Limited.

By contrast, at lower NW concentration, the luminescence of the LED shifted gradually from green to white with increased bias, owing to participation of not only the NW layer but also the carrier transport layers in the carrier recombination processes (Figure 13c, right). Meanwhile, its carrier transport experienced successively FN quantum tunneling, direct quantum tunneling, and direct injection with the increased bias. Bi et al. fabricated CsPbI<sub>3</sub> NW clusters-based LEDs, exhibiting an EQE of 6.2% and record high luminance of 13 644 cd m<sup>-2</sup> for red EL. Meanwhile, the unencapsulated device in ambient conditions possessed a half-lifetime of 13.5 min and 694 h at an initial luminance of 11 500 cd m<sup>-2</sup> and 100 cd m<sup>-2</sup>, respectively.

Polarized LEDs based on MHP NWs have also been demonstrated by Wei et al. through mechanical rubbing.<sup>[199]</sup> Zhang et al. for the first time fabricated 3D spherical LEDs by utilizing CSVG-grown MHP QW arrays, as shown in Figure 13d, left and middle.<sup>[120]</sup> Compared with an ideal Lambertian emission profile for common planar LEDs, the angular emission profile of such a 3D spherical LED showed excellent spatial luminance uniformity in 4 $\pi$  space (Figure 13d, right). Meanwhile, a single LED device in 4-in. wafer size was also demonstrated by them with good uniformity. Fu et al. demonstrated strongly quantum-confined CsPbBr<sub>3</sub> NWs for cyan/sky-blue/pure-blue LEDs via closed space sublimation in ultrasmall pore ( $\approx$ 2.8 nm)

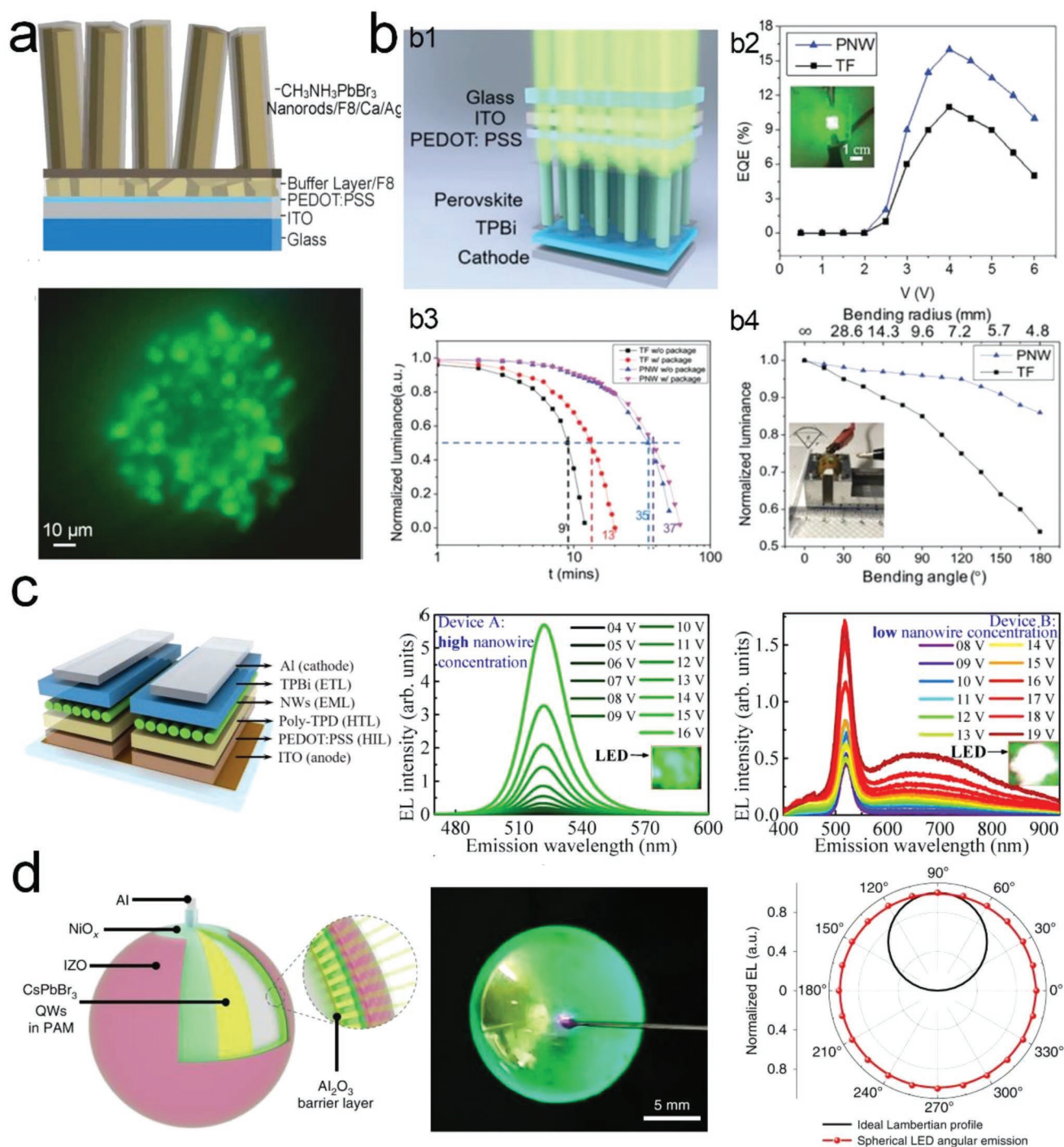


**Figure 13.** MHP NWs for LEDs application: a) vertical MAPbBr<sub>3</sub> NRs based LEDs: schematic illustration of the device structure (top) and EL image of the device (bottom). Reproduced with permission.<sup>[197]</sup> Copyright 2015, American Chemical Society. b) Vertically aligned MHP NW arrays for LEDs: schematic illustration of the LED device structure (b1), EQE curves of the MHP NW and thin-film devices (b2), continuous lighting (at 4 V) stability of the MHP NW and thin-film devices with and without epoxy packaging (b3), and bending test of MHP NW and thin-film devices with different bending angles (b4). Reproduced with permission.<sup>[103]</sup> Copyright 2020, American Chemical Society. c) Horizontal CsPbBr<sub>3</sub> NWs based green–white color switchable LEDs: schematic illustration of the device structure (left), EL spectra of device A (middle) and B (right) under different driven voltages, devices A and B have high and low NWs concentration, respectively. Reproduced with permission.<sup>[198]</sup> Copyright 2021, AIP publishing. d) CsPbBr<sub>3</sub> QW arrays-based spherical LEDs: schematic illustration of the device structure (left), EL image (middle), and angular emission (right) of the spherical device. Reproduced with permission.<sup>[120]</sup> Copyright 2022, Springer Nature Limited.

AAO templates.<sup>[200]</sup> Benefiting from efficient charge injection in the vertically 1D structure, EQE of 7.1%, 3.2%, and 0.9% have been achieved for cyan, sky-blue, and pure-blue LEDs, respectively, with room to optimize in the future. The results reviewed above have demonstrated the promising potential of MHP NWs (QWs) in the future large-area, full-color, and high-performance display and lighting applications.

### 5.5. Re-RAMs

MHPs have come to the fore as switching layers in the Re-RAMs because of the innate hysteresis and innumerable charge/ion transport channels.<sup>[201–205]</sup> Recently, MHP NWs gener-

ated research interest in Re-RAM applications due to more efficient ion transport.<sup>[115,116,206,207]</sup> For instance, Poddar et al. reported MAPbI<sub>3</sub> NWs/QWs-based Re-RAMs with remarkable performance, as shown in Figure 14a.<sup>[115]</sup> Figure 14a1 shows the device structure, where each MHP NW is embedded in the AAO template. When using Ag and Al as top and bottom electrodes, respectively, the Ag/MAPbI<sub>3</sub>/Al Re-RAM device could reach  $6 \times 10^6$  cycles endurance without any notable degradation in ON/OFF ratio, as shown in Figure 14a2. The device also showed ultrafast switching speed (100 ps for SET and RESET) which could be attributed to the fast ionic and electronic mobility in the single-crystalline NWs (Figure 14a3,a4). The diameter of NWs could be flexibly controlled in the range of 10–300 nm. Figure 14a5 shows a device with a device area

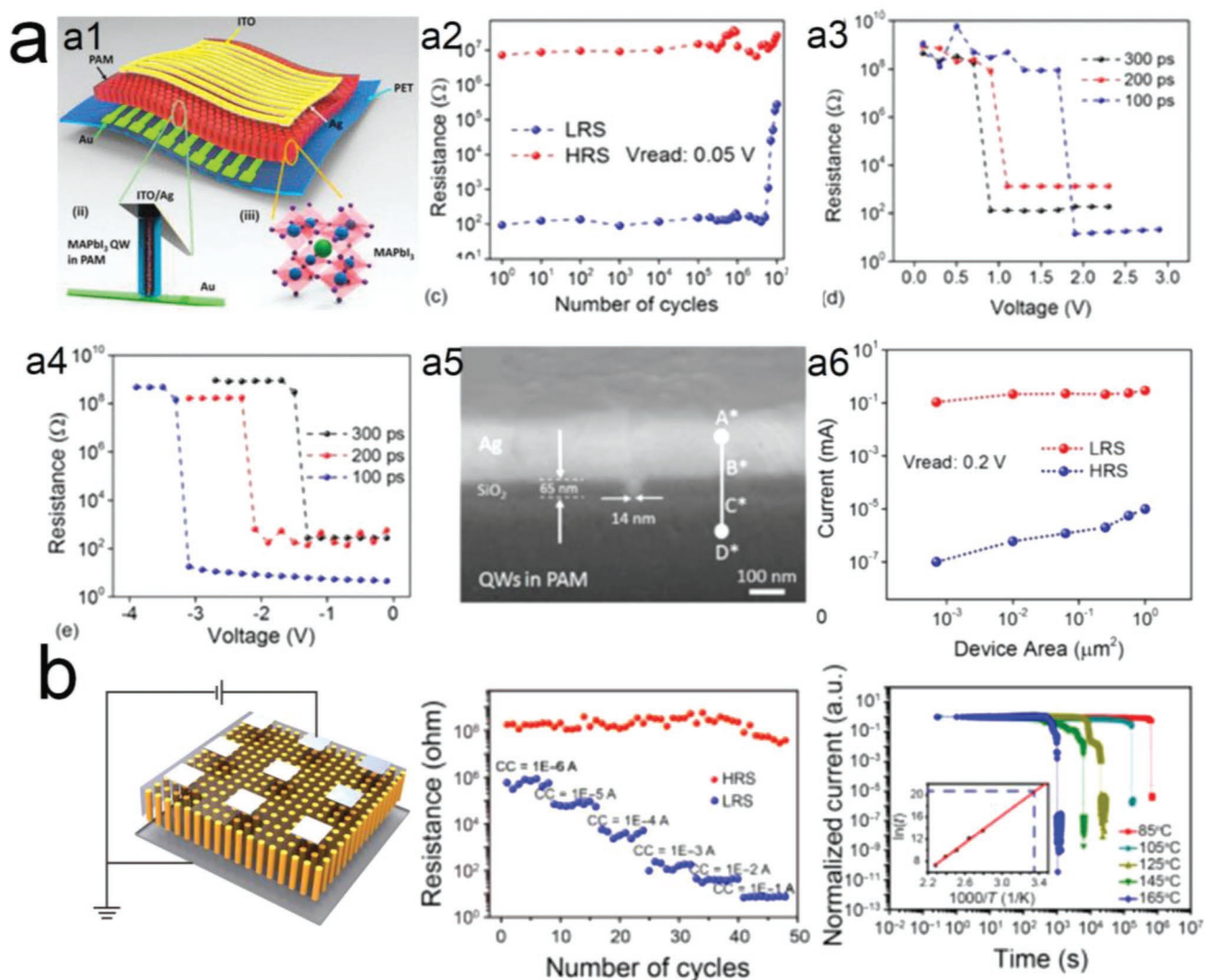


**Figure 14.** MHP NWs for Re-RAM applications: a) vertically aligned MAPbI<sub>3</sub> NWs for ultrafast Re-RAMs with down scalability: schematic illustration of the device structure (a1), endurance study of the distinct resistance levels of the device (a2), writing (a3), and erasing (a4) speed measurements for 180 nm long NWs device exhibiting fastest speed of 100 ps, cross-sectional SEM image of the smallest device with effective areas of 0.000153 μm<sup>2</sup> (a5), and electrical response of the different device sizes fabricated by the FIB technique (a6). Reproduced with permission.<sup>[115]</sup> Copyright 2021, American Chemical Society. b) Vertically aligned MAPbX<sub>3</sub> NWs for ultrafast Re-RAMs with ultralong data retention: schematic illustration of the device structure (left), multilevel resistance states of the devices with different current compliances (middle), and ON state retention time measurement of the devices at different temperatures (right). Reproduced with permission.<sup>[116]</sup> Copyright 2020, American Association for the Advancement of Science.

of 153 nm<sup>2</sup>, which was fabricated by FIB electrode deposition. The low resistance state current decreased less monotonically than the high resistance current with device size downscaling, as shown in Figure 14a6. The retention time of the MAPbX<sub>3</sub> (X = Cl, Br, I) NWs-based Re-RAMs has also been systematically studied by Zhang et al.<sup>[116]</sup> The Ag/MAPbCl<sub>3</sub> NWs/Al-based Re-RAMs showed a typical multilevel switching trait, as shown in Figure 14b, left and middle. The MAPbCl<sub>3</sub> NWs exhibited the longest retention time among different MAPbX<sub>3</sub> NWs. The retention time at different temperatures for MAPbCl<sub>3</sub> NWs-based Re-RAMs is shown in Figure 14b, right. The retention time at room temperature (25 °C) was extrapolated based on the Arrhenius relation ( $\ln(t) \propto E_a/kT$ ), which could reach  $\approx 9 \times 10^8$  s. The outstanding retention performance was attributed to the AAO template passivation which could properly effectively shield the perovskite NWs from the water and oxygen induced attacks.

### 5.6. FETs

As another significant electronic application, perovskite NWs-based FETs have also been reported with good device performance because of low defects density and superior carrier mobility. For instance, Chen et al. reported organic semiconductor and CsPbI<sub>3</sub> NRs bilayer structure for FETs, as schematically shown in Figure 15a, the left figure.<sup>[208]</sup> In such a unique structure, the perovskite NRs work as efficient light absorbers. While the organic semiconductor layer acts as a transport channel for injected photogenerated carriers and provides gate tuning. The output curves ( $I_D-V_D$ ) in the dark state are shown in Figure 15a, the middle figure. The device exhibits p-type transistor characteristics, displaying both linear and saturation regions with a cut-off  $V_G$  of around -40 V. The transfer curves ( $I_D-I_G$ ) of the device with a gate voltage sweeping from -60 to 20 V and a fixed  $V_D$  of -30 V are shown in Figure 15a, the right figure. Obvious photoresponse can be seen from the curves under light illumination. The applied gate voltage can be used to modulate the photosensitive performances of the devices. Meanwhile, with increase in the light power density, the threshold voltage shifts positively because of the photogating effect. Meng et al. also applied the single VLS-grown perovskite (CsPbX<sub>3</sub>, X = Cl, Br, or I) NW to FETs application, with the device transfer and output characteristics shown in Figure 15b.<sup>[100]</sup> A superior hole field-effect mobility of 3.05 cm<sup>2</sup> V<sup>-1</sup> S<sup>-1</sup> is achieved for CsPbI<sub>3</sub> NW-based FETs. The same group also reported unique single-CsPbBr<sub>3</sub>/MoO<sub>3</sub> core-shell NW-based FETs, as shown in the device SEM image and NW schematics in Figure 15c, left and middle, respectively.<sup>[209]</sup> Benefiting from efficient interfacial charge transfer and reduced impurity scattering, a significantly increased hole field-effect mobility of 23.3 cm<sup>2</sup> V<sup>-1</sup> S<sup>-1</sup> is achieved with 10 nm MoO<sub>3</sub> shell, which is better than any mobility value reported for perovskite FETs. It also worth mentioning that the MoO<sub>3</sub> shell can provide excellent surface passivation to the perovskite NW core and hence minimize the diffusion of detrimental water and oxygen molecules, which can obviously improve the air stability of the device. Chen et al. reported heterojunction consisting of organic semiconductor and perovskite NW arrays as

the FET channel, as schematically shown in Figure 15d, left.<sup>[140]</sup> The transfer characteristics of different FETs under dark state are shown in Figure 15d, middle and right. It can be seen that the MAPbI<sub>3</sub>/PDVT-10 and MAPbI<sub>3</sub>/N220 heterojunction-based FETs show strong characteristics of p-type and n-type FET behaviors, respectively, which is attributed to the introduction of organic semiconductors. Those devices are also demonstrated with strong both the light and gate modulation, resulting in a perovskite/organic semiconductor NWs-based hybrid phototransistor with a high light responsivity of 350 A W<sup>-1</sup>. It is clear that high carrier mobility and excellent light response in perovskite NWs demonstrated their potentials in high-performance FETs and phototransistors.

## 6. Conclusions and Perspective

In summary, we have reviewed the recent research progress made on the MHP NWs, divided mainly into four sections: synthesis of NWs, integration for NW arrays, property characterizations, and advanced optoelectronic applications. First, we systematically scrutinized the literatures about the synthesis methods for both organic-inorganic hybrid and all-inorganic perovskite NWs, including solution phase and vapor phase approaches, as well as the top-down techniques. Most of them are facile, up-scalable, and low-cost approaches, which are significantly promising for large-scale fabrications and practical applications. Then, we reviewed the integration methods of MHP NWs to obtain NW arrays, which render them novel nanophotonic properties, and potentials in the high-performance integrated optoelectronics and electronics. Subsequently, we reviewed some significant advantages of MHP NWs over their thin-film counterparts in terms of materials stability and advanced optical properties. Finally, we reviewed the optoelectronic applications of MHP NWs, such as solar cells, PDs, image sensors and bionic eyes, LEDs, Re-RAMs, and FETs. The novel material properties and excellent device performance indisputably promoted MHP NWs to be a research focus in the field of next-generation semiconductor nanomaterials and their practical applications. Considering the further performance improvement and practical applications of MHP NWs-based optoelectronics, especially for solar cells and LEDs, nevertheless, more explorations are needed on both material optimization and device innovations.

In the aspect of materials, on the one hand, for optoelectronic applications, it is a consensus that nonradiative recombination rate limits the maximum achievable efficiency, particularly in solar cells and LEDs. Compared with their thin-film counterpart, MHP NWs have obviously increased specific surface area, which will induce more nonradiative recombination sites and therefore higher surface nonradiative recombination rate. Even though some templates have been demonstrated to macroscopically passivate NWs surface, exploring NWs surface passivation at an atomic level is needed to further reduce the nonradiative recombination rate. On the other hand, MHP QWs with a strong quantum confinement effect and high PLQY are desirable for fabricating high-performance lasers and LEDs. To date, however, very few pieces of literatures have reported MHP QWs for optoelectronic devices. Under such

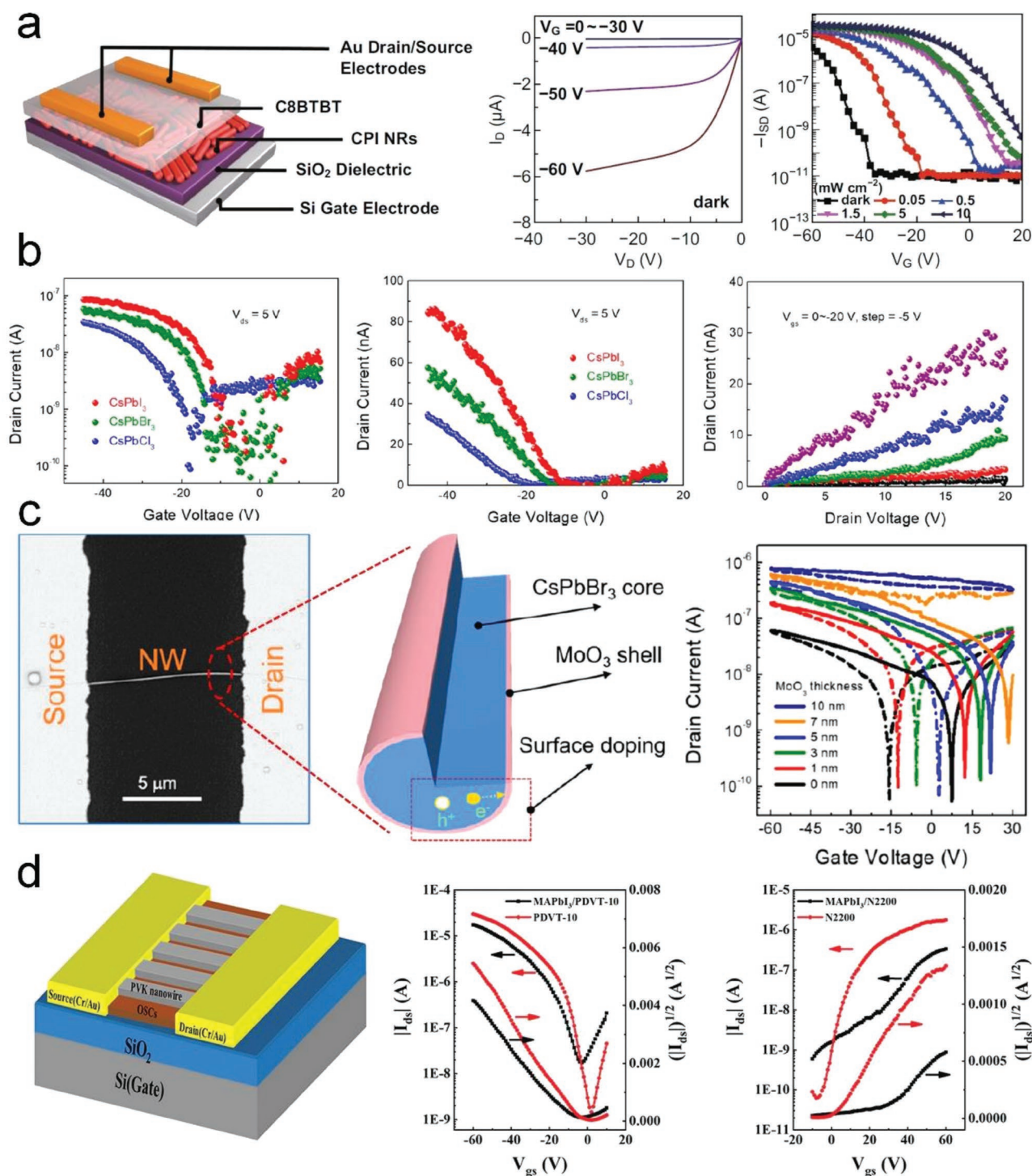


**Figure 15.** MHP NWs for FETs application: a) organic semiconductor and CsPbI<sub>3</sub> NRs bilayer for FETs: schematic of the device (left),  $I_D$ - $V_D$  transistor characteristics of the device in the dark state (middle), and transfer characteristics ( $V_D = -30$  V) under different illumination power densities (right). Reproduced with permission.<sup>[208]</sup> Copyright 2018, Springer Nature Limited. b) Single VLS-grown CsPbX<sub>3</sub> (X = Cl, Br, or I) NW-based FETs: transfer characteristics of single CsPbX<sub>3</sub> NW-based FETs using logarithm (left) and linear (middle) y-coordinate, and output characteristics of single CsPbBr<sub>3</sub> NW-based FETs (right). Reproduced with permission.<sup>[110]</sup> Copyright 2019, American Chemical Society. c) Single CsPbBr<sub>3</sub>/MoO<sub>3</sub> core-shell NW-based FETs: SEM image of the typical device channel (left), schematic of the core-shell NW (middle), and forward (solid lines) and backward (dashed lines) transfer curves with various MoO<sub>3</sub> thickness ( $V_{DS} = 5$  V) (right). Reproduced with permission.<sup>[209]</sup> Copyright 2020, American Chemical Society. d) MAPbI<sub>3</sub>/organic semiconductor NW arrays-based FETs: schematic of the device with a channel consisting of MAPbI<sub>3</sub>/organic semiconductor NW heterojunctions (left), transfer characteristics of devices with different channel structures (middle: pure PDVT-10 with and without MAPbI<sub>3</sub> NWs, right: pure N2200 with and without MAPbI<sub>3</sub> NWs). Reproduced with permission.<sup>[140]</sup> Copyright 2020, The Royal Society of Chemistry.

consideration, the synthesis of MHP QWs and fabrication of QWs-based devices need further optimization to achieve higher device performance. Meanwhile, in the aspect of LEDs device structure, thinking outside the box to fabricate horizontally aligned or core-shell NWs-based LED devices, where light extraction efficiency will be obviously increased, may find a way to maximize the device performance, especially in the aspect of EQE and luminance. Simultaneously, despite the excellent and fast progress from perovskite NWs-based optoelectronics, their application potential has not been unlocked because of a few bottleneck challenges, such as device stability issues, large-area fabrication, etc. For example, for the solution method-grown perovskite NWs based solar cells or LEDs, the fabrication process is limited in glovebox before the device packaging, which obviously hinders the device quantity production for practical applications. Even though some rigid templates have been demonstrated to be adequate for a long material lifetime, the device operation lifetime is still far behind the commercial requirement. Meanwhile, most of current fabrication techniques can only obtain highly ordered perovskite NW arrays in a relatively small area (centimeter scale), restricting their mass production in industry. Even though the growth of highly uniform perovskite QWs on a 4-in. wafer substrate has been demonstrated recently,<sup>[120]</sup> it is only limited to LED applications so far. More exploration of perovskite QWs in various optoelectronics, such as solar cells and FETs, are necessarily needed. Such a promising technique can also inspire researchers to develop other large-scale fabrication methods to promote the practical applications of perovskite NWs. Another potential problem which needs to be addressed before the practical applications is the Pb-induced toxicity issue. Even though substituting Pb with Sn has been demonstrated with thin film optoelectronics to be a potential solution to address it, there are very few reports about Sn-based perovskite NWs to date. The even worse stability of Sn-based perovskite materials in ambient conditions is another great challenge. Device encapsulation should also be well explored in the near future for promoting practical applications of perovskite NWs-based optoelectronics. Finally, some novel types of devices, e.g., electrically pumped lasers, gas sensors, wearable electronics, etc., can also be explored with MHP NWs, which will broaden their practical applications.

In short, MHP NWs have undisputedly set off meteoric research interests and obtained remarkable achievements. However, there is still plenty of room to promote the development of MHP NWs in aspects of both materials and optoelectronic devices, which need cooperative efforts from both academia and industry.

## Acknowledgements

This work was financially supported by Hong Kong Research Grant Council (General Research Fund Project Nos. 16309018, 16214619, and 16205321), Innovation Technology Commission Fund (Project No. GHP/014/19SZ), Shen Zhen Science and Technology Innovation Commission (Project No. JCYJ20170818114107730), Guangdong-Hong Kong-Macao Intelligent Micro-Nano Optoelectronic Technology Joint Laboratory (Grant No. 2020B1212030010), and Foshan Innovative and Entrepreneurial Research Team Program (2018IT100031). The authors also acknowledge the support from the Material Characterization and

Preparation Facility (MCPF), the Center for 1D/2D Quantum Materials, and the State Key Laboratory on Advanced Displays and Optoelectronics Technologies at HKUST.

## Conflict of Interest

The authors declare no conflict of interest.

## Keywords

nanowire arrays, optical properties, optoelectronics, perovskites nanowires, solution phase, stability, templates, vapor phase

Received: May 21, 2022

Revised: July 9, 2022

Published online:

- [1] M. M. Lee, J. Teuscher, T. Miyasaka, T. N. Murakami, H. J. Snaith, *Science* **2012**, *338*, 643.
- [2] Q. Dong, Y. Fang, Y. Shao, P. Mulligan, J. Qiu, L. Cao, J. Huang, *Science* **2015**, *347*, 967.
- [3] S. D. Stranks, G. E. Eperon, G. Grancini, C. Menelaou, M. J. Alcocer, T. Leijtens, L. M. Herz, A. Petrozza, H. J. Snaith, *Science* **2013**, *342*, 341.
- [4] G. Xing, N. Mathews, S. Sun, S. S. Lim, Y. M. Lam, M. Grätzel, S. Mhaisalkar, T. C. Sum, *Science* **2013**, *342*, 344.
- [5] W. J. Yin, T. Shi, Y. Yan, *Adv. Mater.* **2014**, *26*, 4653.
- [6] A. Miyata, A. Mitioglu, P. Plochocka, O. Portugall, J. T.-W. Wang, S. D. Stranks, H. J. Snaith, R. J. Nicholas, *Nat. Phys.* **2015**, *11*, 582.
- [7] K. X. Steirer, P. Schulz, G. Teeter, V. Stevanovic, M. Yang, K. Zhu, J. J. Berry, *ACS Energy Lett.* **2016**, *1*, 360.
- [8] L. Protesescu, S. Yakunin, M. I. Bodnarchuk, F. Krieg, R. Caputo, C. H. Hendon, R. X. Yang, A. Walsh, M. V. Kovalenko, *Nano Lett.* **2015**, *15*, 3692.
- [9] Y.-H. Kim, H. Cho, T.-W. Lee, *Proc. Natl. Acad. Sci. USA* **2016**, *113*, 11694.
- [10] J. S. Manser, J. A. Christians, P. V. Kamat, *Chem. Rev.* **2016**, *116*, 12956.
- [11] J. Huang, Y. Yuan, Y. Shao, Y. Yan, *Nat. Rev. Mater.* **2017**, *2*, 17042.
- [12] Y. Li, W. Yan, Y. Li, S. Wang, W. Wang, Z. Bian, L. Xiao, Q. Gong, *Sci. Rep.* **2015**, *5*, 14485.
- [13] J. J. Yoo, G. Seo, M. R. Chua, T. G. Park, Y. Lu, F. Rotermund, Y.-K. Kim, C. S. Moon, N. J. Jeon, J.-P. Correa-Baena, *Nature* **2021**, *590*, 587.
- [14] M. Kim, J. Jeong, H. Lu, T. K. Lee, F. T. Eickemeyer, Y. Liu, I. W. Choi, S. J. Choi, Y. Jo, H.-B. Kim, *Science* **2022**, *375*, 302.
- [15] NREL, Best research-cell efficiencies, <https://www.nrel.gov/pv/cell-efficiency.html> (accessed: May 2022).
- [16] J. Y. Kim, J.-W. Lee, H. S. Jung, H. Shin, N.-G. Park, *Chem. Rev.* **2020**, *120*, 7867.
- [17] H. Kong, W. Sun, H. Zhou, *J. Semicond.* **2021**, *42*, 101605.
- [18] G. Tang, F. Yan, *J. Semicond.* **2021**, *42*, 101606.
- [19] M. Davis, Z. Yu, *J. Semicond.* **2020**, *41*, 041603.
- [20] Y. Zhu, Q. Zhang, L. Shu, D. Zhang, Z. Fan, *J. Semicond.* **2021**, *42*, 101604.
- [21] M. Kam, Y. Zhu, D. Zhang, L. Gu, J. Chen, Z. Fan, *Solar RRL* **2019**, *3*, 1900050.
- [22] M. Kam, Q. Zhang, D. Zhang, Z. Fan, *Sci. Rep.* **2019**, *9*, 6963.
- [23] L. Dou, Y. M. Yang, J. You, Z. Hong, W. H. Chang, G. Li, Y. Yang, *Nat. Commun.* **2014**, *5*, 5404.

- [24] M. I. Saidaminov, V. Adinolfi, R. Comin, A. L. Abdelhady, W. Peng, I. Dursun, M. Yuan, S. Hoogland, E. H. Sargent, O. M. Bakr, *Nat. Commun.* **2015**, *6*, 8724.
- [25] H. P. Wang, S. Li, X. Liu, Z. Shi, X. Fang, J. H. He, *Adv. Mater.* **2021**, *33*, 2003309.
- [26] M. Ahmadi, T. Wu, B. Hu, *Adv. Mater.* **2017**, *29*, 1605242.
- [27] Y. H. Dong, Y. S. Zou, J. Z. Song, X. F. Song, H. B. Zeng, *J. Mater. Chem. C* **2017**, *5*, 11369.
- [28] J. Zhou, J. Huang, *Adv. Sci.* **2018**, *5*, 1700256.
- [29] Z. Yang, Y. Deng, X. Zhang, S. Wang, H. Chen, S. Yang, J. Khurgin, N. X. Fang, X. Zhang, R. Ma, *Adv. Mater.* **2018**, *30*, 1704333.
- [30] Y. Zhou, X. Qiu, Z. a. Wan, Z. Long, S. Poddar, Q. Zhang, Y. Ding, C. L. J. Chan, D. Zhang, K. Zhou, *Nano Energy* **2022**, *100*, 107516.
- [31] W. Deng, X. Zhang, L. Huang, X. Xu, L. Wang, J. Wang, Q. Shang, S. T. Lee, J. Jie, *Adv. Mater.* **2016**, *28*, 2201.
- [32] L. Gu, M. M. Tavakoli, D. Zhang, Q. Zhang, A. Waleed, Y. Xiao, K. H. Tsui, Y. Lin, L. Liao, J. Wang, Z. Fan, *Adv. Mater.* **2016**, *28*, 9713.
- [33] L. Gu, S. Poddar, Y. Lin, Z. Long, D. Zhang, Q. Zhang, L. Shu, X. Qiu, M. Kam, A. Javey, Z. Fan, *Nature* **2020**, *581*, 278.
- [34] H. Zhu, Y. Fu, F. Meng, X. Wu, Z. Gong, Q. Ding, M. V. Gustafsson, M. T. Trinh, S. Jin, X. Y. Zhu, *Nat. Mater.* **2015**, *14*, 636.
- [35] H. Dong, C. Zhang, X. Liu, J. Yao, Y. S. Zhao, *Chem. Soc. Rev.* **2020**, *49*, 951.
- [36] B. R. Sutherland, E. H. Sargent, *Nat. Photonics* **2016**, *10*, 295.
- [37] S. A. Veldhuis, P. P. Boix, N. Yantara, M. Li, T. C. Sum, N. Mathews, S. G. Mhaisalkar, *Adv. Mater.* **2016**, *28*, 6804.
- [38] K. Lin, J. Xing, L. N. Quan, F. P. G. de Arquer, X. Gong, J. Lu, L. Xie, W. Zhao, D. Zhang, C. Yan, W. Li, X. Liu, Y. Lu, J. Kirman, E. H. Sargent, Q. Xiong, Z. Wei, *Nature* **2018**, *562*, 245.
- [39] Z. G. Xiao, R. A. Kerner, L. F. Zhao, N. L. Tran, K. M. Lee, T. W. Koh, G. D. Scholes, B. P. Rand, *Nat. Photonics* **2017**, *11*, 108.
- [40] D. Ma, K. Lin, Y. Dong, H. Choubisa, A. H. Proppe, D. Wu, Y.-K. Wang, B. Chen, P. Li, J. Z. Fan, *Nature* **2021**, *599*, 594.
- [41] Y. J. Yoon, J. Y. Kim, *J. Semicond.* **2021**, *42*, 101608.
- [42] Q. Zhang, D. Zhang, Y. Fu, S. Poddar, L. Shu, X. Mo, Z. Fan, *Adv. Funct. Mater.* **2020**, *30*, 2002570.
- [43] S. Yakunin, M. Sytnyk, D. Krieger, S. Shrestha, M. Richter, G. J. Matt, H. Azimi, C. J. Brabec, J. Stangl, M. V. Kovalenko, *Nat. Photonics* **2015**, *9*, 444.
- [44] H. Wei, D. DeSantis, W. Wei, Y. Deng, D. Guo, T. J. Savenije, L. Cao, J. Huang, *Nat. Mater.* **2017**, *16*, 826.
- [45] Q. Chen, J. Wu, X. Ou, B. Huang, J. Almutlaq, A. A. Zhumekenov, X. Guan, S. Han, L. Liang, Z. Yi, J. Li, X. Xie, Y. Wang, Y. Li, D. Fan, D. B. L. Teh, A. H. All, O. F. Mohammed, O. M. Bakr, T. Wu, M. Bettinelli, H. Yang, W. Huang, X. Liu, *Nature* **2018**, *561*, 88.
- [46] J. Zhao, L. Zhao, Y. Deng, X. Xiao, Z. Ni, S. Xu, J. Huang, *Nat. Photonics* **2020**, *14*, 612.
- [47] S. Deumel, A. van Breemen, G. Gelinck, B. Peeters, J. Maas, R. Verbeek, S. Shanmugam, H. Akkerman, E. Meulenkaamp, J. E. Huerdler, *Nat. Electron.* **2021**, *4*, 681.
- [48] L. Pan, G. Zhu, *Perovskite Materials: Synthesis, Characterisation, Properties, and Applications*, IntechOpen, London, United Kingdom **2016**.
- [49] M. I. Saidaminov, A. L. Abdelhady, B. Murali, E. Alarousu, V. M. Burlakov, W. Peng, I. Dursun, L. Wang, Y. He, G. Maculan, *Nat. Commun.* **2015**, *6*, 7586.
- [50] D. Shi, V. Adinolfi, R. Comin, M. Yuan, E. Alarousu, A. Buin, Y. Chen, S. Hoogland, A. Rothenberger, K. Katsiev, *Science* **2015**, *347*, 519.
- [51] Y. Lei, Y. Chen, R. Zhang, Y. Li, Q. Yan, S. Lee, Y. Yu, H. Tsai, W. Choi, K. Wang, *Nature* **2020**, *583*, 790.
- [52] A. Feng, X. Jiang, X. Zhang, X. Zheng, W. Zheng, O. F. Mohammed, Z. Chen, O. M. Bakr, *Chem. Mater.* **2020**, *32*, 7602.
- [53] Z. Chen, B. Turedi, A. Y. Alsalloum, C. Yang, X. Zheng, I. Gereige, A. AlSaggaf, O. F. Mohammed, O. M. Bakr, *ACS Energy Lett.* **2019**, *4*, 1258.
- [54] M. Xiao, F. Huang, W. Huang, Y. Dkhissi, Y. Zhu, J. Etheridge, A. Gray-Weale, U. Bach, Y. B. Cheng, L. Spiccia, *Angew. Chem., Int. Ed.* **2014**, *53*, 9898.
- [55] W. Zhang, M. Saliba, D. T. Moore, S. K. Pathak, M. T. Höranter, T. Stergiopoulos, S. D. Stranks, G. E. Eperon, J. A. Alexander-Webber, A. Abate, *Nat. Commun.* **2015**, *6*, 6142.
- [56] A. Sharenko, M. F. Toney, *J. Am. Chem. Soc.* **2016**, *138*, 463.
- [57] G. E. Eperon, S. N. Habisreutinger, T. Leijtens, B. J. Bruijnaers, J. J. van Franeker, D. W. DeQuilettes, S. Pathak, R. J. Sutton, G. Grancini, D. S. Ginger, *ACS Nano* **2015**, *9*, 9380.
- [58] A. Babayigit, J. D'Haen, H.-G. Boyen, B. Conings, *Joule* **2018**, *2*, 1205.
- [59] L. C. Schmidt, A. Pertegás, S. González-Carrero, O. Malinkiewicz, S. Agouram, G. Minguez Espallargas, H. J. Bolink, R. E. Galian, J. Pérez-Prieto, *J. Am. Chem. Soc.* **2014**, *136*, 850.
- [60] A. Dey, J. Ye, A. De, E. Debroye, S. K. Ha, E. Bladt, A. S. Kshirsagar, Z. Wang, J. Yin, Y. Wang, *ACS Nano* **2021**, *15*, 10775.
- [61] F. Yan, J. Xing, G. Xing, L. Quan, S. T. Tan, J. Zhao, R. Su, L. Zhang, S. Chen, Y. Zhao, A. Huan, E. H. Sargent, Q. Xiong, H. V. Demir, *Nano Lett.* **2018**, *18*, 3157.
- [62] J. Xing, F. Yan, Y. Zhao, S. Chen, H. Yu, Q. Zhang, R. Zeng, H. V. Demir, X. Sun, A. Huan, *ACS Nano* **2016**, *10*, 6623.
- [63] L. Polavarapu, B. Nickel, J. Feldmann, A. S. Urban, *Adv. Energy Mater.* **2017**, *7*, 1700267.
- [64] J. Chen, J. Wang, X. Xu, J. Li, J. Song, S. Lan, S. Liu, B. Cai, B. Han, J. T. Pecht, *Nat. Photonics* **2021**, *15*, 238.
- [65] J. Byun, H. Cho, C. Wolf, M. Jang, A. Sadhanala, R. H. Friend, H. Yang, T. W. Lee, *Adv. Mater.* **2016**, *28*, 7515.
- [66] Y. Xu, M. Wang, Y. Lei, Z. Ci, Z. Jin, *Adv. Energy Mater.* **2020**, *10*, 2002558.
- [67] X. Zhang, G. Wu, W. Fu, M. Qin, W. Yang, J. Yan, Z. Zhang, X. Lu, H. Chen, *Adv. Energy Mater.* **2018**, *8*, 1702498.
- [68] Y. Fu, Q. P. Zhang, D. Q. Zhang, Y. Q. Tang, L. Shu, Y. Y. Zhu, Z. Y. Fan, *Adv. Funct. Mater.* **2020**, *30*, 2002913.
- [69] X. Zhang, S. Chen, X. Wang, A. Pan, *Small Methods* **2019**, *3*, 1800294.
- [70] D. Zhang, S. W. Eaton, Y. Yu, L. Dou, P. Yang, *J. Am. Chem. Soc.* **2015**, *137*, 9230.
- [71] M. Shoaib, X. Zhang, X. Wang, H. Zhou, T. Xu, X. Wang, X. Hu, H. Liu, X. Fan, W. Zheng, T. Yang, S. Yang, Q. Zhang, X. Zhu, L. Sun, A. Pan, *J. Am. Chem. Soc.* **2017**, *139*, 15592.
- [72] R. Singh, S. R. Suranagi, S. J. Yang, K. Cho, *Nano Energy* **2018**, *51*, 192.
- [73] C. Zhang, J. Chen, S. Wang, L. Kong, S. W. Lewis, X. Yang, A. L. Rogach, G. Jia, *Adv. Mater.* **2020**, *32*, 2002736.
- [74] G. S. Kumar, R. R. Sumukam, R. K. Rajaboina, R. N. Savu, M. Srinivas, M. Banavath, *ACS Appl. Energy Mater.* **2022**, *5*, 1342.
- [75] Y. Wang, X. Li, J. Song, L. Xiao, H. Zeng, H. Sun, *Adv. Mater.* **2015**, *27*, 7101.
- [76] S. Ananthakumar, J. R. Kumar, S. M. Babu, *J. Photonics Energy* **2016**, *6*, 042001.
- [77] J. Song, J. Li, L. Xu, J. Li, F. Zhang, B. Han, Q. Shan, H. Zeng, *Adv. Mater.* **2018**, *30*, 1800764.
- [78] Q. Shan, C. Wei, Y. Jiang, J. Song, Y. Zou, L. Xu, T. Fang, T. Wang, Y. Dong, J. Liu, *Light: Sci. Appl.* **2020**, *9*, 163.
- [79] R. Yan, D. Gargas, P. Yang, *Nat. Photonics* **2009**, *3*, 569.
- [80] L. N. Quan, J. Kang, C.-Z. Ning, P. Yang, *Chem. Rev.* **2019**.
- [81] M. Spina, M. Lehmann, B. Náfrádi, L. Bernard, E. Bonvin, R. Gaál, A. Magrez, L. Forró, E. Horváth, *Small* **2015**, *11*, 4824.
- [82] J. G. Feng, C. Gong, H. F. Gao, W. Wen, Y. J. Gong, X. Y. Jiang, B. Zhang, Y. C. Wu, Y. S. Wu, H. B. Fu, L. Jiang, X. Zhang, *Nat. Electron.* **2018**, *1*, 404.
- [83] N. Zhou, Y. Bekenstein, C. N. Eisler, D. Zhang, A. M. Schwartzberg, P. Yang, A. P. Alivisatos, J. A. Lewis, *Sci. Adv.* **2019**, *5*, 8141.
- [84] L. Gao, K. Zeng, J. Guo, C. Ge, J. Du, Y. Zhao, C. Chen, H. Deng, Y. He, H. Song, *Nano Lett.* **2016**, *16*, 7446.



- [85] Y. Tong, B. J. Bohn, E. Bladt, K. Wang, P. Müller-Buschbaum, S. Bals, A. S. Urban, L. Polavarapu, J. Feldmann, *Angew. Chem., Int. Ed.* **2017**, 56, 13887.
- [86] M. B. Teunis, A. Jana, P. Dutta, M. A. Johnson, M. Mandal, B. B. Muhoberac, R. Sardar, *Chem. Mater.* **2016**, 28, 5043.
- [87] E. Horvath, M. Spina, Z. Szekrenyes, K. Kamaras, R. Gaal, D. Gachet, L. Forro, *Nano Lett.* **2014**, 14, 6761.
- [88] H. Deng, D. Dong, K. Qiao, L. Bu, B. Li, D. Yang, H.-E. Wang, Y. Cheng, Z. Zhao, J. Tang, *Nanoscale* **2015**, 7, 4163.
- [89] H. Deng, X. Yang, D. Dong, B. Li, D. Yang, S. Yuan, K. Qiao, Y.-B. Cheng, J. Tang, H. Song, *Nano Lett.* **2015**, 15, 7963.
- [90] A. A. Petrov, N. Pellet, J.-Y. Seo, N. A. Belich, D. Y. Kovalev, A. V. Shevelkov, E. A. Goodilin, S. M. Zakeeruddin, A. B. Tarasov, M. Graetzel, *Chem. Mater.* **2017**, 29, 587.
- [91] T. Yang, Y. Zheng, Z. Du, W. Liu, Z. Yang, F. Gao, L. Wang, K.-C. Chou, X. Hou, W. Yang, *ACS Nano* **2018**, 12, 1611.
- [92] D. Zhang, Y. Yu, Y. Bekenstein, A. B. Wong, A. P. Alivisatos, P. Yang, *J. Am. Chem. Soc.* **2016**, 138, 13155.
- [93] D. Zhang, Y. Yang, Y. Bekenstein, Y. Yu, N. A. Gibson, A. B. Wong, S. W. Eaton, N. Kornienko, Q. Kong, M. Lai, *J. Am. Chem. Soc.* **2016**, 138, 7236.
- [94] S. Zhuo, J. Zhang, Y. Shi, Y. Huang, B. Zhang, *Angew. Chem.* **2015**, 127, 5785.
- [95] S. Z. Oener, P. Khoram, S. Brittman, S. A. Mann, Q. Zhang, Z. Fan, S. W. Boettcher, E. C. Garnett, *Nano Lett.* **2017**, 17, 6557.
- [96] M. J. Ashley, M. N. O'Brien, K. R. Hedderick, J. A. Mason, M. B. Ross, C. A. Mirkin, *J. Am. Chem. Soc.* **2016**, 138, 10096.
- [97] C. H. Lin, C. Y. Kang, T. Z. Wu, C. L. Tsai, C. W. Sher, X. Guan, P. T. Lee, T. Wu, C. H. Ho, H. C. Kuo, *Adv. Funct. Mater.* **2020**, 30, 1909275.
- [98] C.-H. Lin, T.-Y. Li, J. Zhang, Z.-Y. Chiao, P.-C. Wei, H.-C. Fu, L. Hu, M.-J. Yu, G. H. Ahmed, X. Guan, *Nano Energy* **2020**, 73, 104801.
- [99] Z. Zhang, K. Suchan, J. Li, C. Hetherington, A. Kiligaris, E. Unger, I. G. Scheblykin, J. Wallentin, *J. Phys. Chem. C* **2021**, 125, 4860.
- [100] S. L. Kwon, Y. U. Jin, B. J. Kim, M. H. Han, G. S. Han, S. Shin, S. Lee, H. S. Jung, *Appl. Surf. Sci.* **2017**, 416, 96.
- [101] H. C. Kwon, A. Kim, H. Lee, D. Lee, S. Jeong, J. Moon, *Adv. Energy Mater.* **2016**, 6, 1601055.
- [102] Z. Zhang, H. Dierks, N. Lamers, C. Sun, K. Nováková, C. Hetherington, I. G. Scheblykin, J. Wallentin, *ACS Appl. Nano Mater.* **2022**, 5, 881.
- [103] Q. Zhang, D. Zhang, L. Gu, K.-H. Tsui, S. Poddar, Y. Fu, L. Shu, Z. Fan, *ACS Nano* **2020**, 14, 1577.
- [104] P. Khoram, S. Z. Oener, Q. Zhang, Z. Fan, E. C. Garnett, *Mol. Syst. Des. Eng.* **2018**, 3, 723.
- [105] S. Ma, S. H. Kim, B. Jeong, H. C. Kwon, S. C. Yun, G. Jang, H. Yang, C. Park, D. Lee, J. Moon, *Small* **2019**, 15, 1900219.
- [106] Z. Zhang, N. Lamers, C. Sun, C. Hetherington, I. G. Scheblykin, J. Wallentin, *Nano Lett.* **2022**, 22, 2941.
- [107] Q. Zhou, J. G. Park, R. Nie, A. K. Thokchom, D. Ha, J. Pan, S. I. Seok, T. Kim, *ACS Nano* **2018**, 12, 8406.
- [108] M. Spina, E. Bonvin, A. Sienkiewicz, B. Náfrádi, L. Forró, E. Horváth, *Sci. Rep.* **2016**, 6, 19834.
- [109] Y. Xiang, X. Mo, X. Li, K. Huang, P. He, G. Dai, J. Yang, *J. Phys. D: Appl. Phys.* **2021**.
- [110] Y. Meng, C. Lan, F. Li, S. Yip, R. Wei, X. Kang, X. Bu, R. Dong, H. Zhang, J. C. Ho, *ACS Nano* **2019**, 13, 6060.
- [111] J. K. Meyers, S. Kim, D. J. Hill, E. E. Cating, L. J. Williams, A. S. Kumbhar, J. R. McBride, J. M. Papanikolas, J. F. Cahoon, *Nano Lett.* **2017**, 17, 7561.
- [112] K. Park, J. W. Lee, J. D. Kim, N. S. Han, D. M. Jang, S. Jeong, J. Park, J. K. Song, *J. Phys. Chem. Lett.* **2016**, 7, 3703.
- [113] A. Waleed, M. M. Tavakoli, L. Gu, Z. Wang, D. Zhang, A. Manikandan, Q. Zhang, R. Zhang, Y. L. Chueh, Z. Fan, *Nano Lett.* **2017**, 17, 523.
- [114] L. L. Gu, D. Q. Zhang, M. Kam, Q. P. Zhang, S. Poddar, Y. Fu, X. L. Mo, Z. Y. Fan, *Nanoscale* **2018**, 10, 15164.
- [115] S. Poddar, Y. Zhang, L. Gu, D. Zhang, Q. Zhang, S. Yan, M. Kam, S. Zhang, Z. Song, W. Hu, *Nano Lett.* **2021**, 21, 5036.
- [116] Y. Zhang, S. Poddar, H. Huang, L. Gu, Q. Zhang, Y. Zhou, S. Yan, S. Zhang, Z. Song, B. Huang, *Sci. Adv.* **2021**, 7, 3788.
- [117] A. Waleed, M. M. Tavakoli, L. L. Gu, S. Hussain, D. Q. Zhang, S. Poddar, Z. Y. Wang, R. J. Zhang, Z. Y. Fan, *Nano Lett.* **2017**, 17, 4951.
- [118] D. Zhang, L. Gu, Q. Zhang, Y. Lin, D. H. Lien, M. Kam, S. Poddar, E. C. Garnett, A. Javey, Z. Fan, *Nano Lett.* **2019**, 19, 2850.
- [119] M. M. Tavakoli, A. Waleed, L. Gu, D. Zhang, R. Tavakoli, B. Lei, W. Su, F. Fang, Z. Fan, *Nanoscale* **2017**, 9, 5828.
- [120] D. Zhang, Q. Zhang, B. Ren, Y. Zhu, M. Abdellah, Y. Fu, B. Cao, C. Wang, L. Gu, Y. Ding, *Nat. Photonics* **2022**, 16, 284.
- [121] E. Oksenberg, A. Merdasa, L. Houben, I. Kaplan-Ashiri, A. Rothman, I. G. Scheblykin, E. L. Unger, E. Joselevich, *Nat. Commun.* **2020**, 11, 489.
- [122] G. Tong, M. Jiang, D. Y. Son, L. K. Ono, Y. Qi, *Adv. Funct. Mater.* **2020**, 30, 2002526.
- [123] M. K. Hossain, R. dos Reis, W. Qarony, Y. H. Tsang, J. C. Ho, K. M. Yu, *J. Mater. Chem. C* **2021**, 9, 3229.
- [124] Z. Wu, J. Chen, Y. Mi, X. Sui, S. Zhang, W. Du, R. Wang, J. Shi, X. Wu, X. Qiu, *Adv. Opt. Mater.* **2018**, 6, 1800674.
- [125] Y. Gao, L. Zhao, Q. Shang, C. Li, Z. Liu, Q. Li, X. Wang, Q. Zhang, *J. Semicond.* **2019**, 40, 052201.
- [126] X. Xu, X. Zhang, W. Deng, L. Huang, W. Wang, J. Jie, X. Zhang, *ACS Appl. Mater. Interfaces* **2018**, 10, 10287.
- [127] J. Chen, Z. Luo, Y. Fu, X. Wang, K. J. Czech, S. Shen, L. Guo, J. C. Wright, A. Pan, S. Jin, *ACS Energy Lett.* **2019**, 4, 1045.
- [128] J. Mao, W. E. Sha, H. Zhang, X. Ren, J. Zhuang, V. A. Roy, K. S. Wong, W. C. Choy, *Adv. Funct. Mater.* **2017**, 27, 1606525.
- [129] F. Cao, W. Tian, M. Wang, H. Cao, L. Li, *Adv. Funct. Mater.* **2019**, 29, 1901280.
- [130] M. S. Alias, Y. Yang, T. K. Ng, I. Dursun, D. Shi, M. I. Saidaminov, D. Priante, O. M. Bakr, B. S. Ooi, *J. Phys. Chem. Lett.* **2016**, 7, 137.
- [131] M. S. Alias, I. Dursun, D. Shi, M. I. Saidaminov, E. M. Diallo, D. Priante, T. K. Ng, O. M. Bakr, B. S. Ooi, *J. Vac. Sci. Technol., B: Nanotechnol. Microelectron.: Mater., Process., Meas., Phenom.* **2015**, 33, 051207.
- [132] Y. Gao, C. Huang, C. Hao, S. Sun, L. Zhang, C. Zhang, Z. Duan, K. Wang, Z. Jin, N. Zhang, *ACS Nano* **2018**, 12, 8847.
- [133] Z. Fan, H. Razavi, J.-w. Do, A. Moriwaki, O. Ergen, Y.-L. Chueh, P. W. Leu, J. C. Ho, T. Takahashi, L. A. Reichertz, *Nat. Mater.* **2009**, 8, 648.
- [134] A. I. Hochbaum, R. Fan, R. He, P. Yang, *Nano Lett.* **2005**, 5, 457.
- [135] W. Lu, C. M. Lieber, *J. Phys. D: Appl. Phys.* **2006**, 39, R387.
- [136] B. Jeong, I. Hwang, S. Cho, E. Kim, S. Cha, J. Lee, H. Kang, S. Cho, H. Choi, C. Park, *ACS Nano* **2016**, 10, 9026.
- [137] P. Liu, X. He, J. Ren, Q. Liao, J. Yao, H. Fu, *ACS Nano* **2017**, 11, 5766.
- [138] Z. Yang, J. Lu, M. ZhuGe, Y. Cheng, J. Hu, F. Li, S. Qiao, Y. Zhang, G. Hu, Q. Yang, *Adv. Mater.* **2019**, 31, 1900647.
- [139] M. Wang, W. Tian, F. Cao, M. Wang, L. Li, *Adv. Funct. Mater.* **2020**, 30, 1909771.
- [140] P.-A. Chen, J. Guo, M. Nouri, Q. Tao, Z. Li, Q. Li, L. Du, H. Chen, Z. Dong, L. Chang, *J. Mater. Chem. C* **2020**, 8, 2353.
- [141] I. Rodriguez, R. Fenollosa, F. Ramiro-Manzano, R. García-Aboal, P. Atienzar, F. J. Meseguer, *Mater. Chem. Front.* **2019**, 3, 1754.
- [142] R. Huang, D.-H. Lin, J.-Y. Liu, C.-Y. Wu, D. Wu, L.-B. Luo, *Sci. China Mater.* **2021**, 64, 2497.
- [143] W. Deng, L. Huang, X. Xu, X. Zhang, X. Jin, S.-T. Lee, J. Jie, *Nano Lett.* **2017**, 17, 2482.
- [144] S. Pan, H. Zou, A. C. Wang, Z. Wang, J. Yu, C. Lan, Q. Liu, Z. L. Wang, T. Lian, J. Peng, *Angew. Chem., Int. Ed.* **2020**, 59, 14942.

- [145] Q. Hu, H. Wu, J. Sun, D. Yan, Y. Gao, J. Yang, *Nanoscale* **2016**, *8*, 5350.
- [146] L. Lee, J. Baek, K. S. Park, Y.-E. Lee, N. K. Shrestha, M. M. Sung, *Nat. Commun.* **2017**, *8*, 15882.
- [147] G. Chen, J. Feng, H. Gao, Y. Zhao, Y. Pi, X. Jiang, Y. Wu, L. Jiang, *Adv. Funct. Mater.* **2019**, *29*, 1808741.
- [148] Y. Zhao, Y. Qiu, H. Gao, J. Feng, G. Chen, L. Jiang, Y. Wu, *Adv. Mater.* **2020**, *32*, 1905298.
- [149] H. Gao, J. Feng, Y. Pi, Z. Zhou, B. Zhang, Y. Wu, X. Wang, X. Jiang, L. Jiang, *Adv. Funct. Mater.* **2018**, *28*, 1804349.
- [150] Z. Liu, C. Zhang, X. Liu, A. Ren, Z. Zhou, C. Qiao, Y. Guan, Y. Fan, F. Hu, Y. S. Zhao, *Adv. Sci.* **2021**, *8*, 2102065.
- [151] M. Chen, J. Yang, Z. Wang, Z. Xu, H. Lee, H. Lee, Z. Zhou, S. P. Feng, S. Lee, J. Pyo, *Adv. Mater.* **2019**, *31*, 1904073.
- [152] X. Wang, M. Shoaib, X. Wang, X. Zhang, M. He, Z. Luo, W. Zheng, H. Li, T. Yang, X. Zhu, *ACS Nano* **2018**, *12*, 6170.
- [153] H. Lu, Y. Liu, P. Ahlawat, A. Mishra, W. R. Tress, F. T. Eickemeyer, Y. Yang, F. Fu, Z. Wang, C. E. Avalos, *Science* **2020**, *370*, eabb8985.
- [154] J. Xing, X. F. Liu, Q. Zhang, S. T. Ha, Y. W. Yuan, C. Shen, T. C. Sum, Q. Xiong, *Nano Lett.* **2015**, *15*, 4571.
- [155] Y. Fu, H. Zhu, A. W. Schrader, D. Liang, Q. Ding, P. Joshi, L. Hwang, X. Zhu, S. Jin, *Nano Lett.* **2016**, *16*, 1000.
- [156] A. P. Schlaus, M. S. Spencer, K. Miyata, F. Liu, X. Wang, I. Datta, M. Lipson, A. Pan, X.-Y. Zhu, *Nat. Commun.* **2019**, *10*, 265.
- [157] S. W. Eaton, M. Lai, N. A. Gibson, A. B. Wong, L. Dou, J. Ma, L.-W. Wang, S. R. Leone, P. Yang, *Proc. Natl. Acad. Sci. USA* **2016**, *113*, 1993.
- [158] Y. Fu, H. Zhu, C. C. Stoumpos, Q. Ding, J. Wang, M. G. Kanatzidis, X. Zhu, S. Jin, *ACS Nano* **2016**, *10*, 7963.
- [159] Z. Liu, Q. Shang, C. Li, L. Zhao, Y. Gao, Q. Li, J. Chen, S. Zhang, X. Liu, Y. Fu, *Appl. Phys. Lett.* **2019**, *114*, 101902.
- [160] A. P. Pushkarev, V. I. Korolev, D. I. Markina, F. E. Komissarenko, A. Naujokaitis, A. Drabavicius, V. Pakstas, M. Franckevicius, S. A. Khubezhov, D. A. Sannikov, *ACS Appl. Mater. Interfaces* **2018**, *11*, 1040.
- [161] Q. Zhang, Y. Lin, H. Tang, X. Sun, B. Cao, D. Zhang, S. Poddar, Z. Fan, *IEEE J. Electron Devices Soc.* **2021**, *9*, 1215.
- [162] Q. Shang, C. Li, S. Zhang, Y. Liang, Z. Liu, X. Liu, Q. Zhang, *Nano Lett.* **2020**, *20*, 1023.
- [163] E. Oksenberg, C. Fai, I. G. Scheblykin, E. Joselevich, E. L. Unger, T. Unold, C. Hages, A. Merdasa, *Adv. Funct. Mater.* **2021**, *31*, 2010704.
- [164] M. Law, J. Goldberger, P. Yang, *Annu. Rev. Mater. Res.* **2004**, *34*, 83.
- [165] B. M. Kayes, H. A. Atwater, N. S. Lewis, *J. Appl. Phys.* **2005**, *97*, 114302.
- [166] E. Garnett, P. Yang, *Nano Lett.* **2010**, *10*, 1082.
- [167] M. D. Kelzenberg, S. W. Boettcher, J. A. Petykiewicz, D. B. Turner-Evans, M. C. Putnam, E. L. Warren, J. M. Spurgeon, R. M. Briggs, N. S. Lewis, H. A. Atwater, *Nat. Mater.* **2010**, *9*, 239.
- [168] S.-F. Leung, M. Yu, Q. Lin, K. Kwon, K.-L. Ching, L. Gu, K. Yu, Z. Fan, *Nano Lett.* **2012**, *12*, 3682.
- [169] M. M. Tavakoli, K.-H. Tsui, Q. Zhang, J. He, Y. Yao, D. Li, Z. Fan, *ACS Nano* **2015**, *9*, 10287.
- [170] J.-H. Im, J. Luo, M. Franckevičius, N. Pellet, P. Gao, T. Moehl, S. M. Zakeeruddin, M. K. Nazeeruddin, M. Grätzel, N.-G. Park, *Nano Lett.* **2015**, *15*, 2120.
- [171] J.-F. Liao, W.-G. Li, H.-S. Rao, B.-X. Chen, X.-D. Wang, H.-Y. Chen, D.-B. Kuang, *Sci. China Mater.* **2017**, *60*, 285.
- [172] W. Raja, A. Bozzola, F. De Angelis, R. P. Zaccaria, in *Perovskite Nanowire Based Multijunction Solar Cell, Optical Nanostructures and Advanced Materials for Photovoltaics*, Optical Society of America, Washington, DC **2015**, p. PTh3B. 2.
- [173] C.-Y. Chang, B.-C. Tsai, M.-Z. Lin, Y.-C. Huang, C.-S. Tsao, *J. Mater. Chem. A* **2017**, *5*, 22824.
- [174] K. Xiao, C. Cui, P. Wang, P. Lin, Y. Qiang, L. Xu, J. Xie, Z. Yang, X. Zhu, X. Yu, *Nanotechnology* **2018**, *29*, 065401.
- [175] C. Soci, A. Zhang, X.-Y. Bao, H. Kim, Y. Lo, D. Wang, *J. Nanosci. Nanotechnol.* **2010**, *10*, 1430.
- [176] R. Agarwal, C. Lieber, *Appl. Phys. A* **2006**, *85*, 209.
- [177] M. Nehra, N. Dilbaghi, G. Marrazza, A. Kaushik, R. Abolhassani, Y. K. Mishra, K. H. Kim, S. Kumar, *Nano Energy* **2020**, *76*, 104991.
- [178] A. Pan, X. Zhu, in *Semiconductor Nanowires*, Elsevier, New York **2015**, p. 327.
- [179] S. Yip, L. Shen, J. C. Ho, *J. Semicond.* **2019**, *40*, 111602.
- [180] D. Ghoshal, T. Wang, H. Z. Tsai, S. W. Chang, M. Crommie, N. Koratkar, S. F. Shi, *Adv. Opt. Mater.* **2019**, *7*, 1900039.
- [181] E. Oksenberg, E. Sanders, R. Popovitz-Biro, L. Houben, E. Joselevich, *Nano Lett.* **2018**, *18*, 424.
- [182] X. Li, Y. Meng, R. Fan, S. Fan, C. Dang, X. Feng, J. C. Ho, Y. Lu, *Nano Res.* **2021**, *14*, 4033.
- [183] D. Wu, H. Zhou, Z. Song, M. Zheng, R. Liu, X. Pan, H. Wan, J. Zhang, H. Wang, X. Li, *ACS Nano* **2020**, *14*, 2777.
- [184] D. Zhang, Y. Zhu, Q. Zhang, B. Ren, B. Cao, Q. Li, S. Poddar, Y. Zhou, X. Qiu, Z. He, *Nano Lett.* **2022**, *22*, 2589.
- [185] I. M. Asuo, P. Fourmont, I. Ka, D. Gedamu, S. Bouzidi, A. Pignolet, R. Nechache, S. G. Cloutier, *Small* **2019**, *15*, 1804150.
- [186] Y. Li, Z. Shi, L. Wang, Y. Chen, W. Liang, D. Wu, X. Li, Y. Zhang, C. Shan, X. Fang, *Mater. Horiz.* **2020**, *7*, 1613.
- [187] P. C. Zhu, S. Gu, X. P. Shen, N. Xu, Y. L. Tan, S. D. Zhuang, Y. Deng, Z. D. Lu, Z. L. Wang, J. Zhu, *Nano Lett.* **2016**, *16*, 871.
- [188] M. Sun, Q. Fang, Z. Zhang, D. Xie, Y. Sun, J. Xu, W. Li, T. Ren, Y. Zhang, *ACS Appl. Mater. Interfaces* **2018**, *10*, 7231.
- [189] D. Dong, H. Deng, C. Hu, H. Song, K. Qiao, X. Yang, J. Zhang, F. Cai, J. Tang, H. Song, *Nanoscale* **2017**, *9*, 1567.
- [190] M. Yu, D. Zhang, Y. Xu, J. Lin, C. Yu, Y. Fang, Z. Liu, Z. Guo, C. Tang, Y. Huang, *J. Colloid Interface Sci.* **2022**, *608*, 2367.
- [191] G. Li, R. Gao, Y. Han, A. Zhai, Y. Liu, Y. Tian, B. Tian, Y. Hao, S. Liu, Y. Wu, *Photonics Res.* **2020**, *8*, 1862.
- [192] S. Chen, S. Li, S. Peng, Y. Huang, J. Zhao, W. Tang, X. Guo, *J. Semicond.* **2018**, *39*, 013001.
- [193] D. Wang, Y. Mei, G. Huang, *J. Semicond.* **2018**, *39*, 011002.
- [194] T. Cheng, Y. Wu, X. Shen, W. Lai, W. Huang, *J. Semicond.* **2018**, *39*, 015001.
- [195] S. Kundu, D. Richtsmeier, A. Hart, V. Yeddu, Z. Song, G. Niu, D. Thrithamarassery Gangadharan, E. Dennis, J. Tang, O. Voznyy, *Adv. Opt. Mater.* **2022**, 2200516.
- [196] L. Li, S. Ye, J. Qu, F. Zhou, J. Song, G. Shen, *Small* **2021**, *17*, 2005606.
- [197] A. B. Wong, M. Lai, S. W. Eaton, Y. Yu, E. Lin, L. Dou, A. Fu, P. Yang, *Nano Lett.* **2015**, *15*, 5519.
- [198] W. Wu, T. Liang, H. Wu, B. Fan, Y. Zhang, J. Fan, *Appl. Phys. Lett.* **2021**, *119*, 033505.
- [199] Y. Wei, Y. Xu, Q. Wang, J. Wang, H. Lu, J. Zhu, *Chem. Commun.* **2020**, *56*, 5413.
- [200] Y. Fu, S. Poddar, B. Ren, Y. Xie, Q. Zhang, D. Zhang, B. Cao, Y. Tang, Y. Ding, X. Qiu, *ACS Nano* **2022**, *16*, 8388.
- [201] K. Kang, H. Ahn, Y. Song, W. Lee, J. Kim, Y. Kim, D. Yoo, T. Lee, *Adv. Mater.* **2019**, *31*, 1804841.
- [202] J. Di, J. Du, Z. Lin, S. Liu, J. Ouyang, J. Chang, *InfoMat* **2021**, *3*, 293.
- [203] K. Kang, W. Hu, X. Tang, *J. Phys. Chem. Lett.* **2021**, *12*, 11673.
- [204] C. Zhang, Y. Li, C. Ma, Q. Zhang, *Small Sci.* **2022**, *2*, 2100086.
- [205] E. J. Yoo, M. Lyu, J. H. Yun, C. J. Kang, Y. J. Choi, L. Wang, *Adv. Mater.* **2015**, *27*, 6170.
- [206] S. Poddar, Y. Zhang, Z. Chen, Z. Ma, Y. Fu, Y. Ding, C. L. J. Chan, Q. Zhang, D. Zhang, Z. Song, *Nanoscale Horiz.* **2022**, *7*, 759.
- [207] S. Poddar, Z. Chen, Z. Ma, Y. Zhang, C. L. J. Chan, B. Ren, Q. Zhang, D. Zhang, G. Shen, H. Zeng, *Adv. Intell. Syst.* **2022**, *4*, 2200065.
- [208] Y. Chen, X. Wu, Y. Chu, J. Zhou, B. Zhou, J. Huang, *Nano-Micro Lett.* **2018**, *10*, 57.
- [209] Y. Meng, Z. Lai, F. Li, W. Wang, S. Yip, Q. Quan, X. Bu, F. Wang, Y. Bao, T. Hosomi, *ACS Nano* **2020**, *14*, 12749.



**Daquan Zhang** is currently a research associate at the Department of Electronic and Computer Engineering (ECE) at the Hong Kong University of Science and Technology (HKUST). He achieved his Ph.D. degree in ECE from HKUST in 2020, and B.Eng. degree in Microelectronics from Wuhan University in 2014. His current research focus is on nanophotonics in perovskite nanowires/quantum wires, and their applications in optoelectronic devices.



**Qianpeng Zhang** is currently a research assistant professor at the Department of ECE in HKUST. He achieved his Ph.D. degree in ECE from HKUST in 2019, M.Phil. degree in ECE from HKUST in 2015, and B.Eng. degree in Optoelectronic Information Engineering from Huazhong University of Science and Technology in 2012. His current research focus is on light extraction in perovskite LEDs, nanophotonics in perovskite nanowires, and perovskite nanowires-based optoelectronic devices.



**Yiyi Zhu** is currently a postdoctoral fellow at the Department of ECE in HKUST. She received her Ph.D. degree in ECE from HKUST in 2022, and bachelor and master degrees in Materials Science and Engineering from Central South University in 2011 and 2014, respectively. Her research focuses on developing highly efficient and stable perovskite photovoltaics.



**Leilei Gu** is an associate professor at Shanghai Jiao Tong University. He received his B.S. and M.S. degrees in Physical Electronics from Fudan University, Shanghai, China, in 2008 and 2011, respectively. He received his Ph.D. degree in the Department of ECE from HKUST, Hong Kong, in 2016. From 2016 to 2020, he worked as a postdoctoral fellow at HKUST. His research focuses on biomimetic optoelectronic systems based on nanomaterials/structures.



**Zhiyong Fan** is a professor at the Department of Electronic and Computer Engineering, HKUST. He is a fellow of the Royal Society of Chemistry and a founding member of The Hong Kong Young Academy of Sciences. His interests are in the design and fabrication of novel nanostructures and nanomaterials for high-performance optoelectronics, energy harvesting devices, and sensors.